ACS NANO

www.acsnano.org

ARTICLE

Leveraging Diffusion Kinetics to Reverse Propane/Propylene Adsorption in Zeolitic Imidazolate Framework-8

Linghe Yang,[⊥] Ying Liu,[⊥] Fang Zheng,* Fuxing Shen, Baojian Liu, Rajamani Krishna,* Zhiguo Zhang, Qiwei Yang, Qilong Ren, and Zongbi Bao*

Cite This: *ACS Nano* 2024, 18, 3614−3626

Read Online

ACCESS | Metrics & More | Article Recommendations | Supporting Information

ABSTRACT: The separation challenge posed by propylene/propane mixtures arises from their nearly identical molecular sizes and physicochemical properties. Metal−organic frameworks (MOFs) have demonstrated potential in addressing this challenge through the precision tailoring of pore sizes and surface chemistry. However, introducing modifications at the molecular level remains a considerable hurdle. This work presents an approach to reversibly tune the propylene/propane adsorption preference in zeolitic imidazolate framework-8 (ZIF-8) by manipulating the particle size and gas flow rate. Systematically increasing the ZIF-8 crystals from 9 to 224 μm restricts propane diffusion, thereby reversing its preferential adsorption over propylene. Furthermore, raising the gas flow rate of mixed propylene/propane shifts the rate-determining breakthrough step from thermodynamic equilibrium to kinetics, again reversing the adsorption preference in a particular ZIF-8 sample. We propose "dynamic selectivity ($S_d(t)$)" as a concept that incorporates both thermodynamic and kinetic factors to elucidate these unexpected findings. Moreover, the driving force equation, grounded on the concept of $S_d(t)$, has improved the precision and stability of the computational simulation for fixed-bed adsorption processes. This work underscores the potential of diffusion-based modulation, implemented through manageable external changes, as a viable strategy to optimize separation performance in porous adsorbent materials.

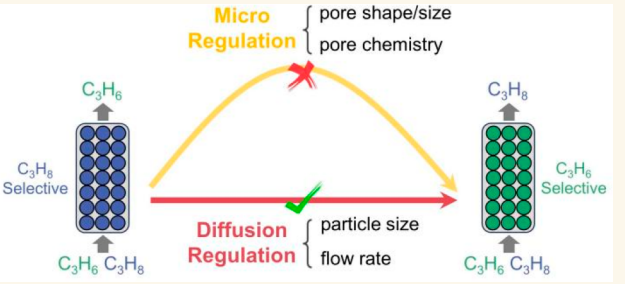

KEYWORDS: *Adsorption, Metal−organic frameworks, ZIF-8, Propane, Propylene, Kinetic separations*

Propylene, an indispensable raw material in the chemical sector, is primarily obtained from naphtha steam cracking and propane dehydrogenation processes that inevitably yield mixtures inclusive of propane and other impurities.[1,2] The separation of propylene-propane binary mixtures poses a daunting challenge due to their near-identical molecular sizes and physical properties.[3,4] Traditional distillation methods, operating at high-pressure and low-temperature, necessitate over 100 stages, given the marginal difference in the boiling points of propylene (225.46 K) and propane (231.02 K).[5,6] Alternatively, adsorption separation methods offer a more benign, energy-efficient, and cost-effective solution, as they circumvent phase changes.[7−10]

Metal−organic frameworks (MOFs), a class of crystalline hybrid porous materials, have attracted tremendous interest for adsorption-based separations owing to their highly ordered, tunable pore structures.[11−18] Several strategies have been employed to separate propane/propylene mixtures using MOFs, with each component's preferential adsorption achieved by adjusting the framework affinity.[19−22] Despite their similar sizes, propylene is slightly smaller along certain directions (Figure S1), enabling kinetic separations through precise pore size control.[23−26] Some flexible MOFs display thermoresponsive gate-opening specific to propylene.[27,28] Ideal molecular sieving of propylene can be realized in MOFs like KAUST-7 via ligand and metal substitution.[29,30] However, tailoring pore architectures and chemistries to match adsorbate properties remains enormously difficult.[31,32]

In fixed bed adsorption processes, both thermodynamic and kinetic factors are in play, with particle size and gas flow rate significantly influencing gas-phase diffusion behavior on the solid phase (intracrystalline and external diffusion).[33,34,54,55]

Received: November 15, 2023
Revised: January 3, 2024
Accepted: January 8, 2024
Published: January 16, 2024

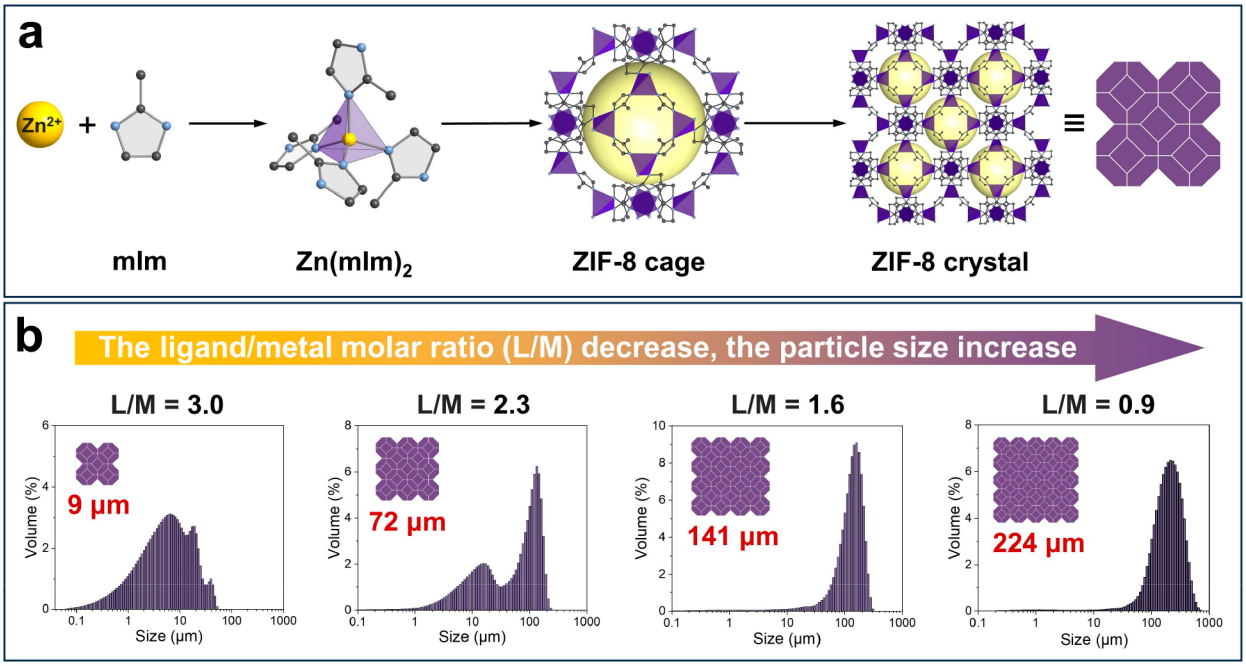

Figure 1. (a) Schematic illustration of the ZIF-8 synthesis process (mIm = 2-methylimidazole). Color scheme for atoms: C, gray; N, blue; Zn, yellow; the H atoms are omitted for clarity. (b) Particle size distribution curves for ZIF-8 samples with varying grain sizes: ZIF-8-9 μm, ZIF-8-72 μm, ZIF-8-141 μm, and ZIF-8-224 μm.

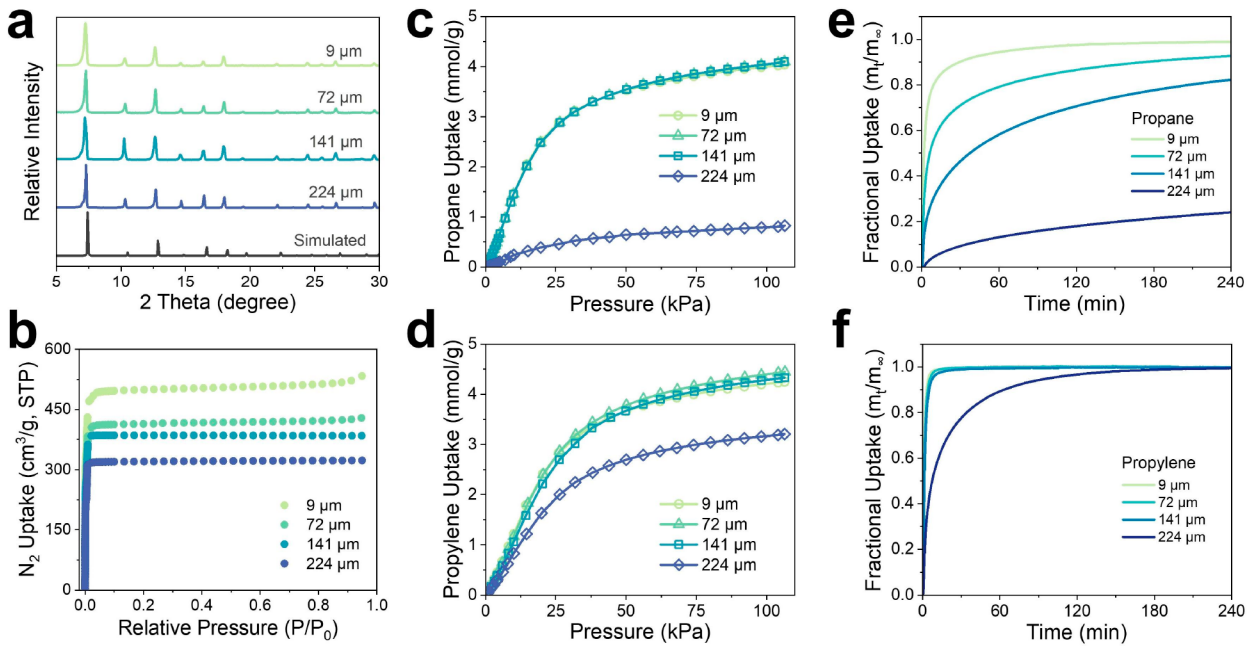

Figure 2. (a) Powder X-ray diffraction (PXRD) patterns. (b) N_2 adsorption isotherms measured at 77 K. (c) Propane adsorption isotherms. (d) Propylene adsorption isotherms for ZIF-8 samples with varying grain sizes. Kinetic uptake curves of (e) propane and (f) propylene at 10 kPa and 298 K for ZIF-8 samples with varying grain sizes.

Importantly, managing the adsorbent size and gas flow rate in fixed bed adsorption processes is more feasible than crafting porous materials at the molecular level.[56,57]

Zeolitic imidazolate frameworks (ZIFs) ingeniously blend the robustness of zeolites with the tunability characteristic of MOFs.[35−40] Zeolitic imidazolate framework-8 (ZIF-8), in particular, has been rigorously explored for adsorption applications, thanks to its convenient synthesis, affordability, and durable structure.[41−47] The cation-free, nonpolar frameworks of ZIF-8 demonstrate a more potent binding affinity toward propane,[48−50] with numerous studies observing a thermodynamic adsorption preference for propane over propylene.[48,51,52] However, Li et al. delved into the potential for kinetic separation of propylene/propane using large ZIF-8 crystals, which demonstrated a preference for propylene.[53] Motivated by this research, we embarked on a journey to probe the feasibility of reversing adsorption preference through macroscopic regulation of particle size and gas flow rate,

https://doi.org/10.1021/acsnano.3c11385
ACS Nano 2024, 18, 3614−3626

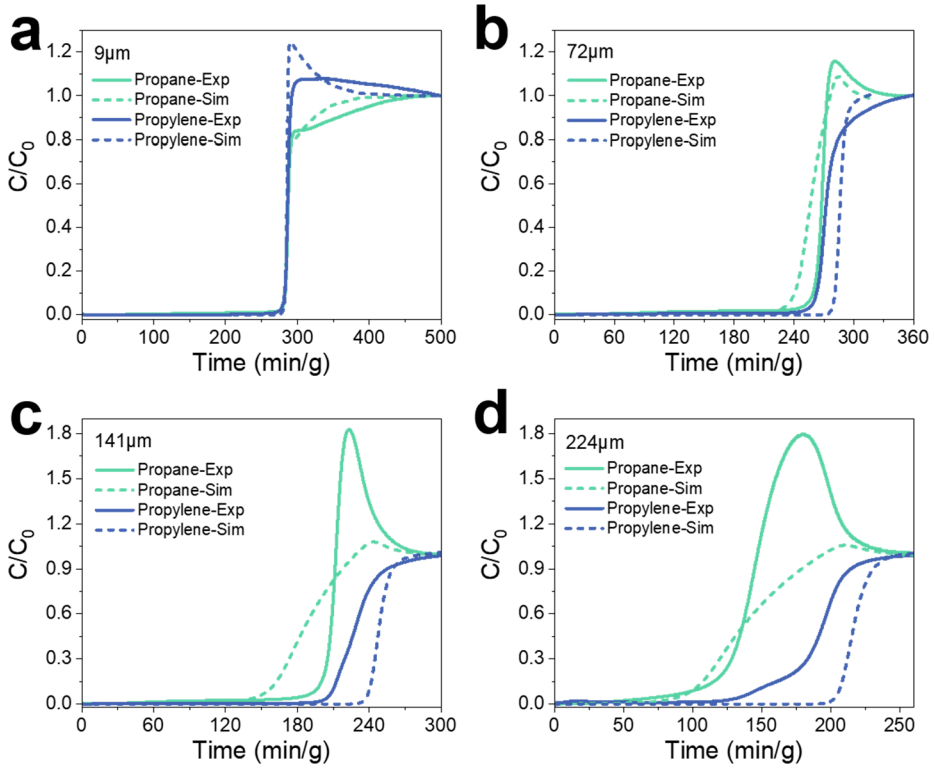

Figure 3. Experimental and simulated breakthrough curves of equimolar binary propane-propylene mixtures for ZIF-8 samples at 298 K with varying grain sizes: (a) 9 μm, (b) 72 μm, (c) 141 μm, and (d) 224 μm.

leveraging the antagonistic interplay between adsorption and diffusion.

In this study, we report the documentation of a selectivity reversal phenomenon in ZIF-8 for equimolar propylene/propane breakthrough experiments, achieved by manipulating the particle size and gas flow rate. By increasing the ZIF-8 particle size, we successfully limited the intracrystalline diffusion of propane within the material, thereby triggering a preferential adsorption reversal from propane to propylene. Furthermore, we were able to invert the adsorption preference by regulating the mixed gas flow rate in ZIF-8 samples with a given particle size. The breakthrough simulation results confirm the viability of reversing the adsorption preference through the control of particle size and flow rate. Following these findings, we introduce the concept of dynamic selectivity ($S_d(t)$) to elucidate these seldom-observed breakthrough phenomena. Within the breakthrough simulation, we developed a driving force equation in the form of an interpolation function (IF) rooted in the $S_d(t)$ concept. In comparison to conventional models, our model demonstrates superior solution accuracy and stability. Given the similar physical processes at work, we propose dynamic selectivity as an efficient and direct method to understand adsorption behavior in microporous materials and enhance the theoretical model for fixed bed breakthrough scenarios.

RESULTS AND DISCUSSION

A comprehensive set of ZIF-8 samples, with average particle sizes spanning from 9 to 224 μm (Figure 1a), was successfully synthesized via a solvothermal reaction (detailed in the Supporting Information (SI)). Analysis of the grain size distribution curves revealed a direct relationship between the ligand/metal molar ratio and the average particle size. Lowering the ligand:metal molar ratio (L/M) led to an increase in the ZIF-8 particle size (Figure 1b). Intriguingly, the medium-sized ZIF-8 (72 μm) presented two peaks in the grain size distribution curve, likely a result of inconsistent growth rates along the bottle wall and bottom. However, this did not disrupt the relative relationship of the average particle size. SEM images (Figure S2) confirmed that the synthesis method generated ZIF-8 particles across all of the size ranges. PXRD results underscored the high crystallinity of ZIF-8 materials of varying particle sizes with peak angles aligning closely with the simulated XRD pattern (Figure 2a). BET surface area calculations for ZIF-8 particles of 9, 72, 141, and 224 μm yielded values of 2151, 1804, 1725, and 1372 m^2/g, respectively (Figure S3). The lower BET surface area values for larger particles could be ascribed to the reduced external surface area and prolonged diffusion time (Figure 2b).

We recorded the single-component adsorption isotherms of propane and propylene on ZIF-8 particles of varied sizes at 298 K (Figure 2c,d). Despite their different sizes, the ZIF-8 particles showed comparable thermodynamic properties. At low pressure (10 kPa), propane exhibited a higher adsorption capacity (1.47 mmol/g) than propylene (1.22 mmol/g), whereas at atmospheric pressure (100 kPa), the scenario reversed, with the adsorption capacity for propane (3.99 mmol/g) falling below that for propylene (4.20 mmol/g). The low-pressure adsorption capacity more accurately reflects the affinity between the adsorbent and gas molecules (Figure S5). ZIF-8 displayed a slightly stronger affinity for propane over propylene, with the calculated Henry's selectivity for propane/propylene at 1.13, aligning well with literature reports (1.8).[48] Notably, ZIF-8 particles measuring 224 μm showed a significant decrease in adsorption capacity for both propane and propylene, likely due to a lesser specific surface area and extended gas diffusion time. Increasing the test's equilibrium time (up to 10-fold)

https://doi.org/10.1021/acsnano.3c11385
ACS Nano 2024, 18, 3614−3626

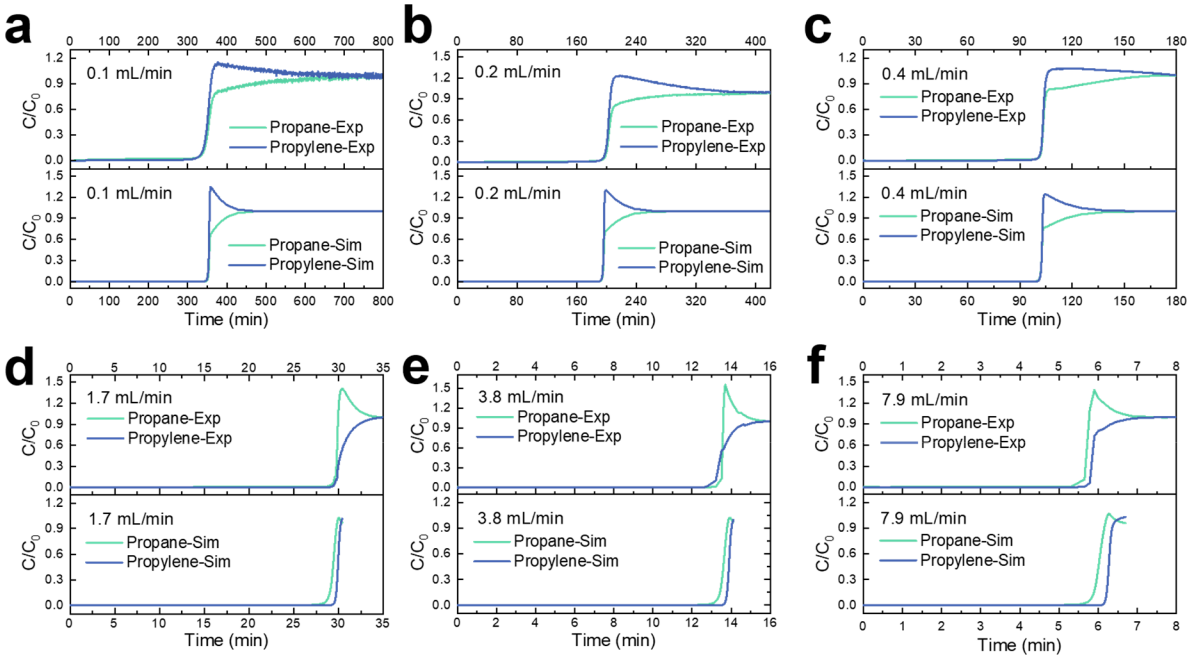

Figure 4. Experimental and simulated breakthrough curves of equimolar binary propane-propylene mixtures for ZIF-8-9 μm at 298 K with flow rates of (a) 0.1 (b) 0.2, (c) 0.4, (d) 1.7, (e) 3.8, and (f) 7.9 mL/min.

significantly enhanced the adsorption capacity of propane, but still far away from the adsorption equilibrium (Figure S4). To precisely ascertain the equilibrium adsorption capacity for propane and propylene, we adjusted the adsorption capacity and diffusion equilibrium time for low pressure (10 kPa), breakthrough partial pressure (50 kPa), and atmospheric pressure (100 kPa) using kinetic uptake plots (Figures S6–S9 and Table S1). The thermogravimetric curves (Figure S16) before degassing (blue lines) show a weight decrease commencing at 373 K, signifying the removal of solvent from the samples. After the degassing treatment, the weight of the ZIF-8 samples with particle sizes of 9, 72, and 141 μm (green lines) remains stable, indicating that the solvent has been effectively removed. However, for the ZIF-8-224 μm sample, a notable weight loss is observed after the temperature exceeds 500 K, suggesting incomplete removal of the solvent. This observation underlines that larger particle sizes could potentially affect the kinetics of the adsorption and desorption of different guest molecules. Therefore, we have taken rigorous steps to ensure complete degassing (473 K for 5 days) to minimize any potential impact on our adsorption results as much as possible.

The kinetic adsorption test (Figure 2e,f) showed that the results of ZIF-8 with varying particle sizes deviated from the ideal scenario (Table S2). The diffusion of propane in ZIF-8 was relatively predictable, with different radii resulting in a diffusion time constant (D/r^2) for ZIF-8-9 and ZIF-8-224 μm that differed by approximately 1000 times. As the particle size increased, the diffusion of propane in ZIF-8 significantly slowed. Due to the instrument's noninstantaneous boosting process, the measurement of the diffusion coefficient (D) of the fast diffusion component (propylene) of different ZIF-8 particles resulted in an error of over 100 times. Particularly for ZIF-8-9 μm, ZIF-8-72 μm and ZIF-8-141 μm, the measured diffusion time constant was virtually identical, suggesting that the test results were primarily controlled by the instrument's pressure boosting process. Therefore, for the calibration of diffusion coefficients and related simulated calculations, test results of large particle materials, which are closer to intrinsic diffusion, are often chosen.[54−56] Despite potential inaccuracies in these adsorption tests, it can be concluded that the slower rate of propane adsorption could trigger a reversal of breakthrough selectivity.

A series of fixed-bed breakthrough experiments and the corresponding simulations substantiated our hypothesis. An equimolar propylene/propane mixture flowed through a column of identical specification, packed with ZIF-8 particles of different sizes, at a flow rate of 0.4 mL/min (Figure 3). With the particle size increase, the elution order of distinct components shifts. The breakthrough selectivity of propylene/propane escalated from 0.9 (ZIF-8-9 μm) to 2.0 (ZIF-8-224 μm) (Table S3). Simulations based on our established model[33,57,58] were able to reproduce these reverse results, simply by adjusting the particle size (r) while maintaining a consistent set of diffusion coefficients for the entire simulation campaign, demonstrating an agreement with the experimental curves. Note that the discrepancy between the experimental and simulated breakthrough curves becomes more pronounced as particle size and the flow rate increase. This divergence is primarily attributed to the breakthrough curve rolling up, indicative of competitive adsorption effects among the components. Video animations of the breakthrough simulations presented in Figure 3a,b,c,d are available for viewing in the SI. The x-axis represents the dimensionless distance along the fixed bed. The y-axis shows the molar concentrations of propylene and propane. The video animations show the development of the gas phase concentration fronts as they traverse the bed. Larger ZIF-8 particles demonstrated a more pronounced diffusion effect, resulting in a smaller diffusional time constant (D/r^2), which in turn stimulated intracrystalline diffusion and led to the earlier exit of propane from the fixed-bed column. Conversely, for ZIF-8-9 μm, its larger diffusion time constant diminishes the role of intracrystalline diffusion, and as D/r^2 approaches infinity, the diffusion limitation is eliminated. The adsorption of both propylene and propane on ZIF-8-9 μm swiftly reaches

https://doi.org/10.1021/acsnano.3c11385
ACS Nano 2024, 18, 3614−3626

equilibrium, yielding a breakthrough result that closely mirrors the static adsorption results.

The intricate kinetics involved in the breakthrough experiment, which encompasses both the inflow and outflow of the mixed gas, ultimately tether the process to diffusion regulation. This regulation can exert a significant influence on the separation process. A series of breakthrough experiments were conducted using a column packed with ZIF-8-9 μm (Figure 4), at diverse flow rates. We discerned a fascinating correlation: as the flow rate escalated, the breakthrough selectivity for propylene/propane improved, increasing from 0.9 at 0.1 mL/min to 1.1 at 7.9 mL/min under constant particle size conditions (Table S4). Breakthrough simulation results, based on reliable input data on intracrystalline diffusivity, also confirmed that altering the flow rate (interstitial velocity of feed gas) can indeed reverse the adsorption preference. A plausible interpretation of this phenomenon could be that an increase in flow rate pivots the primary determinant of the column breakthrough experiment from thermodynamics to kinetics. This, in turn, modifies the adsorption preference. However, those conventional indicators-IAST selectivity/Henry's selectivity, kinetic selectivity-only partially rationalize the breakthrough effect, focusing either on the adsorption equilibrium time or the low-pressure adsorption capacity. These indicators exhibit two substantial limitations: first, they do not adequately illustrate the relative influence of thermodynamics and kinetics in the breakthrough experiment; second, they predominantly measure material properties, largely overlooking independent variables such as flow rate that determines the gas-particle contact time.

We noticed that the intracrystalline diffusion process of gases in materials during both the kinetic adsorption test and the breakthrough experiment is very similar (Figure 5a), which provides a potential elucidation for the observed reversal phenomenon. Thus, we propose the concept of dynamic selectivity ($S_d(t)$, see eq 1) based on the results of intracrystalline diffusion from the kinetic adsorption test and a rudimentary assumption of external diffusion. This concept consolidates both thermodynamic and kinetic factors, yet it does not explicitly express pure thermodynamic (e.g., Henry's constant, K) or kinetic indicators (e.g., intracrystalline diffusivity, D).

$$S_d(t) = \frac{n_A(t)}{n_B(t)} \tag{1}$$

Wherein, t denotes the breakthrough equilibrium time, n_A and n_B represent the adsorption capacity pertaining to the kinetic adsorption curves (under breakthrough partial pressure) of components A and B, respectively, at that particular time.

In the context of dynamic selectivity, the adsorption preference is constrained to 1. We postulate that the intracrystalline diffusion time, as applied to dynamic selectivity, is approximately commensurate with the equilibrium time of the breakthrough experiment. This serves to indicate the dynamic equilibrium state at a specific flow rate. Dynamic selectivity provides a predictive model for the reversal phenomenon instigated by alterations in the flow rate (Figure 5b). Adsorption reversal is anticipated to occur when the breakthrough equilibrium time ranges between 20 and 110 min (with $S_d(t)$ values spanning from 0.97 to 1.03). This prediction aligns notably well with the time frame observed empirically, which extends from 35 to 180 min. This observation tentatively validates the reliability of using $S_d(t)$ to estimate a material's

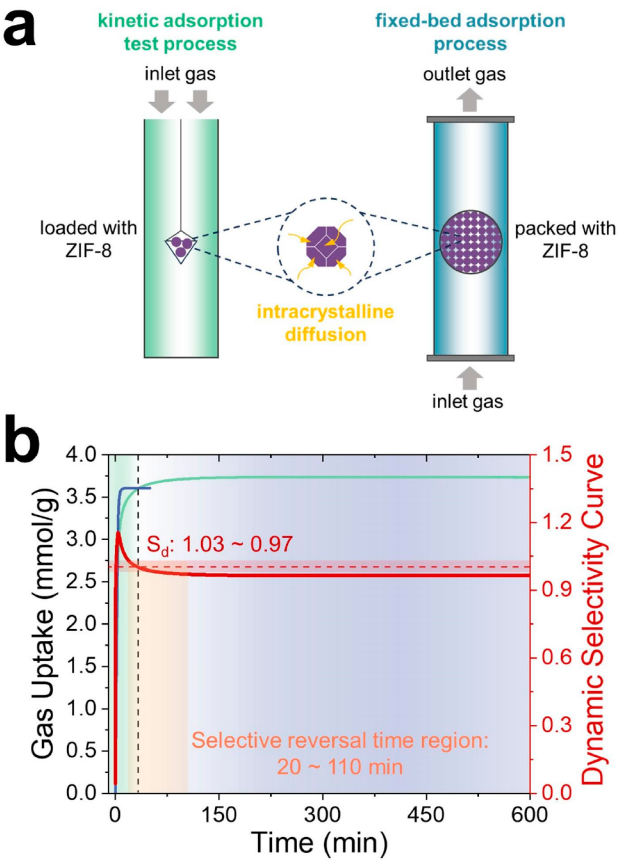

Figure 5. (a) A schematic illustration highlighting the parallelism between the intracrystalline diffusion process of gas during kinetic adsorption testing and the fixed-bed adsorption process. (b) Depiction of kinetic uptake curves for propane (green) and propylene (blue) in ZIF-8-9 μm, subjected to a breakthrough partial pressure of 50 kPa. The corresponding dynamic selectivity curve is also illustrated (red).

separation performance in an actual fixed-bed breakthrough experiment.

The breakthrough model encapsulates our understanding of the fixed-bed adsorption process. Therefore, it is essential to incorporate the concept of $S_d(t)$ into the breakthrough model to enhance our comprehension of the process and yield more precise and consistent simulation results. Given our assumption of similarity in the intracrystalline diffusion process between two tests, we performed a straightforward differential treatment on the kinetic adsorption curves (the adsorption capacity−time (q−t) relationship) of a specific particle size under breakthrough partial pressure. We then transformed the independent variables to the adsorption capacity. This can be numerically converted into the driving force equation ($\partial q/\partial t$-q relationship, Figure 6a,b), which we represent using an interpolation function (IF) equation. In this way, the single-particle adsorption results in a fixed bed, obtained through the integration (reverse processing) of the IF equation, aligns with the results of the kinetic adsorption test. We selected universally recognized models and assumptions for other conditions, such as external diffusion (see Supporting Information for details). The breakthrough results of the IF model, based on the $S_d(t)$ concept, are shown in Figure 6c,d, which are transformed into the form of $q-t$. The termination point of each curve symbolizes the adsorbents' total adsorption uptake at the breakthrough equilibrium.

https://doi.org/10.1021/acsnano.3c11385
ACS Nano 2024, 18, 3614−3626

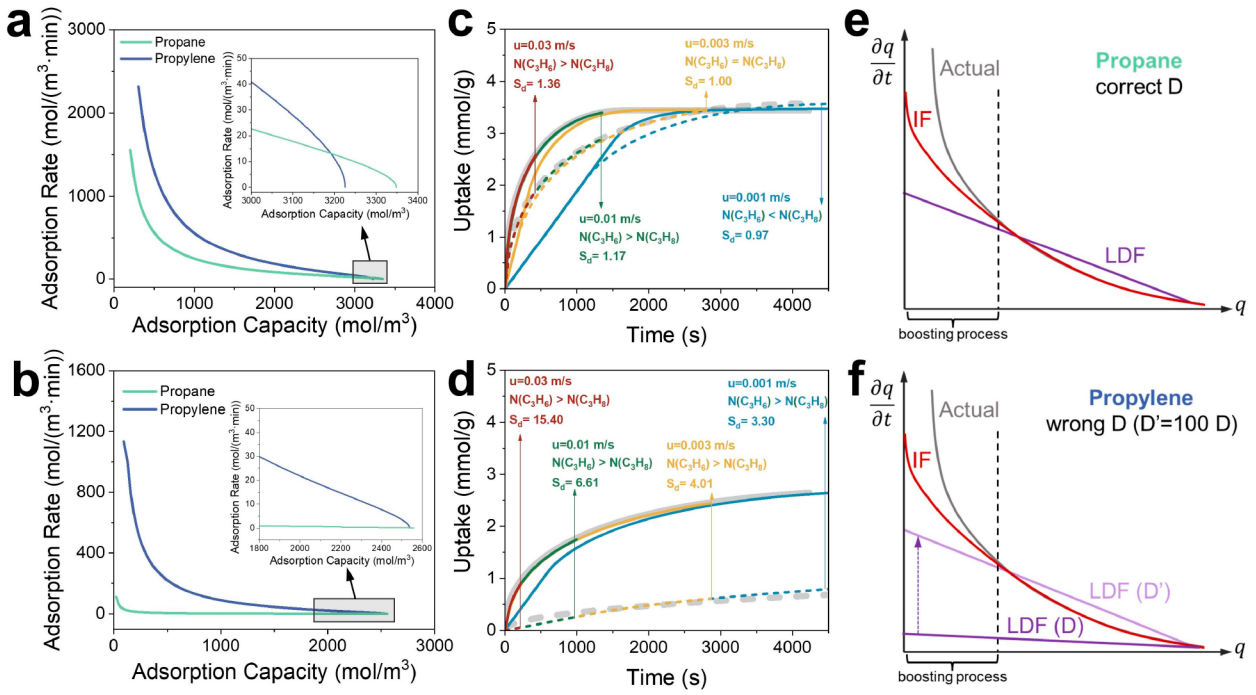

Figure 6. An interpolation function illustrating the relationship between the adsorption rate and adsorption capacity, derived from the simulated kinetic uptake curve at 50 kPa for(a) ZIF-8-9 μm and (b) ZIF-8-224 μm. A comparison of breakthrough simulation results for propylene (solid lines) and propane (dash-dot lines) with the input kinetic uptake curves (gray lines) for (c) ZIF-8-9 μm and (d) ZIF-8-224 μm. A comparative analysis of actual and simulated results was done using the interpolation function (IF) equation and the classic linear driving force (LDF) equation for (e) propane and (f) propylene.

Notably, our model successfully reproduced the flow-rate-induced adsorption reversal after input of the kinetic adsorption test results of ZIF-8-9 μm, a feat that conventional breakthrough models failed to achieve. They could only reproduce the selectivity reversal results after inserting the correct diffusion coefficient (i.e., increasing the propylene diffusion coefficient by more than 2 orders of magnitude).

Such discrepancies in the accuracy of results generated using the same flawed data incite further discussion of the construction of the breakthrough model. In this context, we turn our attention to the classic linear driving force (LDF) equation, frequently employed to depict intracrystalline diffusion, as an exemplar for comparison (Figure 6e, f). It is crucial to acknowledge that, despite the adsorption rate in the low-loading zone significantly exceeding the set value of all models (tending toward infinity when the load is zero), this discrepancy exerts minimal influence on the overarching results. The primary divergence between the IF curve and the true intracrystalline diffusion curve originates from the boost stage. The phenomenon of "limited diffusion", exhibited during the boost stage, causes the IF curve to fall beneath the true diffusion curve within the low load zone. However, congruence between the IF curve and the true diffusion curve manifests upon completion of the boost stage (around 3 min), a precise alignment that persists within the more impactful high load zone, a feat unattainable by generic driving force equations.

When accurate diffusion coefficients (such as that for propane) are provided, both the LDF and IF curves exhibit a strong alignment with the true diffusion curve, implying a high degree of simulation accuracy. On the contrary, when fed with erroneous kinetic results, LDF predictions deviate by an order of magnitude (over 100-fold in this case), a systemic error. In this study, the propylene adsorption rate was significantly underestimated, forestalling the possibility of a reversal, a stark departure from our experimental findings. Paradoxically, the IF curve, maintaining its alignment with the true diffusion curve in the high load zone, remained relatively unaffected. A comprehensive analysis corroborates that the IF equation, premised on the $S_d(t)$ concept, outperforms traditional driving force equations in terms of both accuracy and stability.

Furthermore, it is important to note that both kinetic adsorption testing and breakthrough experimentation fundamentally involve "limited diffusion". However, given the more formalized expression of external diffusion in breakthrough simulations, we can leverage the simulation results to adjust the external diffusion in kinetic adsorption tests, thereby enhancing the predictive power of the breakthrough separation performance under specific operational conditions. As an illustrative instance, in Figure 5b, ZIF-8-9 μm demonstrates a significant adsorption hysteresis (0−900 s) under an inlet linear velocity of 0.001 m/s. By decelerating the rate of the pressure increase during kinetic adsorption tests, we can simulate external diffusion more accurately. It is crucial to bear in mind that real-life breakthrough experiments may be influenced by factors such as the column pressure drop and competitive adsorption between components. These factors, deemed inconsequential in our experiments, were subsequently disregarded. Nonetheless, if these factors prove to be significant in other scenarios, then we can incorporate relevant existing models or assumptions into our model for a more holistic depiction.

CONCLUSIONS

In summary, this study presents the demonstration of completely reversing and tuning the propylene/propane adsorption preference in ZIF-8 through systematic changes in particle size and gas flow rate-reliable external parameters from

https://doi.org/10.1021/acsnano.3c11385
ACS Nano 2024, 18, 3614−3626

both experimental and simulation perspectives. Solely enlarging the ZIF-8 crystals restricts propane diffusion, reversing its preferential adsorption over propylene in breakthrough experiments and simulations. Moreover, raising the flow rate of mixed propylene/propane pivots the breakthrough process from thermodynamic equilibrium to kinetic adsorption, again reversing the selectivity for a given ZIF-8 sample. Breakthrough simulation verifies the dramatic impacts of particle size and flow rate on uptake and selectivity during the breakthrough process. In light of these observations, we propose "dynamic selectivity" as a concept to elucidate the breakthrough phenomena, offering a direct and effective approach to understand adsorption behavior in microporous materials. Our work lays a foundation for enhancing the accuracy and stability of computational simulations and correcting the fixed bed breakthrough theoretical model. This research provides a method for the future exploration of diffusion-based modulation as a versatile strategy for improving separation performance in porous adsorbent materials.

METHODS

Materials. All chemicals were purchased from commercial suppliers without further purification. Zinc nitrate hexahydrate ($Zn(NO_3)_2 \cdot 6H_2O$, 99%) and N,N-dimethylformamide (99.5%) were purchased from Sinopharm Chemical Reagents Co., Ltd. 2-methylimidazole (98%) was purchased from Aladdin. N_2 (99.999%), C_3H_6 (99.999%), C_3H_8 (99.999%), and a gas mixture of C_3H_6/C_3H_8 (50/50, v/v) were obtained from Jingong Co., Ltd. (China) and used for all measurements.

Synthesis of ZIF-8-9 μm. $Zn(NO_3)_2 \cdot 6H_2O$ (5.96 g, 20 mmol) and 2-methylimidazole (4.926 g, 60 mmol) were dissolved in N,N-dimethylformamide (400 mL). The mixture was put into a glass bottle and transferred into an oven under 413 K for 3 days. White crystals were obtained, washed with deionized water three times, and soaked in deionized water three times over 3 days (1 day each) for solvent exchange.

Synthesis of ZIF-8-72 μm. $Zn(NO_3)_2 \cdot 6H_2O$ (5.96 g, 20 mmol) and 2-methylimidazole (3.774 g, 46 mmol) were dissolved in N,N-dimethylformamide (400 mL). The mixture was put into a glass bottle and transferred into an oven under 413 K for 3 days. White crystals were obtained, washed with deionized water three times, and soaked in deionized water three times over 3 days (1 day each) for solvent exchange.

Synthesis of ZIF-8-141 μm. $Zn(NO_3)_2 \cdot 6H_2O$ (5.96 g, 20 mmol) and 2-methylimidazole (2.622 g, 32 mmol) were dissolved in N,N-dimethylformamide (400 mL). The mixture was put into a glass bottle and transferred into an oven under 413 K for 3 days. White crystals were obtained, washed with deionized water three times, and soaked in deionized water three times over 3 days (1 day each) for solvent exchange.

Synthesis of ZIF-8-224 μm. $Zn(NO_3)_2 \cdot 6H_2O$ (5.96 g, 20 mmol) and 2-methylimidazole (1.470 g, 18 mmol) were dissolved in N,N-dimethylformamide (400 mL). The mixture was put into a glass bottle and transferred into an oven under 413 K for 3 days. White crystals were obtained, washed with deionized water three times, and soaked in deionized water three times over 3 days (1 day each) for solvent exchange.

Powder X-ray Diffraction Analysis (PXRD). PXRD data were collected on an X'Pert3 powder diffractometer (PANalytical) with Cu Kα emission radiation (λ = 1.540598 Å), and the operating power was 40 kV, 30 mA. The scan range of 2θ was 2° to 60° with a scan step size of 0.02°. The simulated PXRD pattern was obtained from a CSV file in the Cambridge Crystallographic Data Centre.

Particle Size Distribution Analysis. Particle size distribution data were collected on a Beckman Coulter LS13320 laser particle size analyzer tested in the range of 0.017−2000 μm.

Scanning Electron Microscope (SEM). The scanning electronic microscope (SEM) was performed on a Hitachi SU-8010 after gold puttering for 60 s.

Thermogravimetric Analysis (TGA). The thermogravimetric data were obtained by using a TA-Q500 thermogravimetric analyzer. The experiments were performed under a nitrogen atmosphere, employing a temperature range of 323 to 873 K and a heating rate of 10 K/min.

Gas Adsorption Measurements. Adsorption isotherm data were collected on the Micromeritics ASAP 2020 adsorption apparatus. Around 150 mg of sample prepared according to the above methods was used for the gas adsorption measurement. The outgassing was performed under vacuum at 473 K for 5 days, and the free space was filled with nitrogen gas. The single-component adsorption isotherms were performed at a temperature of 298 K (C_3H_8 and C_3H_6) and 77 K (N_2) and pressure from 0 to 1.0 bar. The dead space of the system was determined by helium.

Kinetic Adsorption Tests. The kinetic adsorption profiles were measured on an Intelligent Gravimetric Analyzer (IGA001, Hiden, U.K.), which uses a gravimetric technique to accurately measure the transient gas uptake as a function of time under various operating conditions. For each test, about 50 mg of ZIF-8 was loaded into the sample basket, and then the system was outgassed at 473 K for 5 days before the dynamic gas sorption measurements. The adsorption kinetics was obtained by measuring mass change at a given temperature and 1000, 500, or 100 mbar at 298 K, and the pressure was boosted by introducing the target gas into the sample chamber from 0 to 1000 mbar at 200 mbar/min, from 0 to 500 mbar at 150 mbar/min or from 0 to 100 mbar at 100 mbar/min. After each test, the chamber was backfilled with the target gas to 1000 mbar and the sample was replaced by a new sample for the next test.

Breakthrough Experiments. Typically, a certain number of samples (0.36 g of ZIF-8-9 μm, 0.42 g of ZIF-8-72 μm, 0.54 g of ZIF-8-141 μm, and 0.74 g of ZIF-8-224 μm, respectively) were activated (outgassed at 473 K for 5 days) before being packed into a stainless steel HPLC column (4.6 mm I.D. × 50 mm). A stream of He flow was introduced into the column to further purge the materials before the breakthrough experiments. The experimental breakthrough experiments were conducted under the flow of a gas mixture of C_3H_6/C_3H_8 (50/50, *v*/*v*). The mixed gas was introduced with different flow rates (7.9, 3.8, 1.7, 0.8, 0.4, 0.2, and 0.1 mL/min) at 298 K, and the outlet gas passing through the column was analyzed by using a Hiden HPR-20 EGA mass spectrometer for continuous sampling gas analysis. After every breakthrough measurement, the column was regenerated with a He gas flow (20 mL/min) at 423 K for 12 h, and then, other breakthrough experiments were conducted using the same column with the regenerated ZIF-8 tested at different flow rates.

Kinetic Selectivity Calculation. The kinetic selectivity β_{ij} is defined as

$$\beta_{ij} = D_i'/D_j' \tag{S1}$$

Where, β_{ij} is the kinetic selectivity, $D'(D_c/r_c^2)$ is the diffusion time constant. The diffusion time constant $D'(D_c/r_c^2)$ can be extracted by correlating the fractional adsorption uptake curves with the following micropore diffusion model:

$$\frac{m_t}{m_\infty} \approx \frac{6}{r_c}\sqrt{\frac{D_c t}{\pi}} \left(\frac{m_t}{m_\infty} < 0.3\right) \tag{S2}$$

Where, m_t is the gas uptake at time t, m_∞ is the gas uptake at equilibrium, D_c is the internal diffusivity of gas molecules in porous media, and r_c is the radius of the equivalent spherical particle.

Henry's Selectivity Calculation. Henry's selectivity reflects the gas separation performance under low-pressure. The single-component sorption isotherms of propylene and propane under low-pressure (<3.0 kPa) are dealt with linear fitting (Figure S5). The slope of the fitted straight line is the Henry's coefficient of the component. Then, Henry's selectivity is calculated by the equation:

https://doi.org/10.1021/acsnano.3c11385
ACS Nano 2024, 18, 3614−3626

$$\text{Henry's selectivity} = \frac{\text{Henry's coefficent of propane}}{\text{Henry's coefficient of propylene}} \quad \text{(S3)}$$

Breakthrough Selectivity Calculation. In this work, breakthrough selectivity is obtained by integrating the breakthrough adsorption curve. The adsorbed amount q_i of gas component i can be calculated from the breakthrough curves by the equation:

$$q_i = \frac{F_i \times t_0 - V_{\text{dead}} - \int_0^{t_0} F_e \Delta t}{m} \quad \text{(S4)}$$

Where, q_i (cm^3/g) is the amount of adsorbed component i, F_i (cm^3/min) is the influent flow rate of the specific gas, t_0 (min) is the breakthrough equilibration time, V_{dead} (cm^3) is the dead volume of the system, F_e (cm^3/min) is the effluent flow rate of the specific gas, and m (g) is the mass of the adsorbents.

Therefore, the breakthrough selectivity can be calculated by the equation:

$$\text{breakthrough selectivity} = \frac{\text{absorbed amount of propylene}}{\text{absorbed amount of propane}} \quad \text{(S5)}$$

Transient Breakthrough Simulations. We summarize below the simulation methodology used to perform transient breakthrough calculations for fixed bed adsorbers (see schematics in Figures S12 and Figure S13). The simulation methodology is the same as used in our earlier publications.[1−5] For an n-component gas mixture in plug flow through a fixed bed maintained under isothermal conditions, the molar concentrations in the gas phase at any position and instant of time are obtained by solving the following set of partial differential equations for each of the species i in the gas mixture[3,6−8]

$$\frac{\partial c_i(t, z)}{\partial t} + \frac{\partial (v(t, z) c_i(t, z))}{\partial z} + \frac{1-\varepsilon}{\varepsilon}\rho \frac{\partial \bar{q}_i(t, z)}{\partial t} = 0;\ i = 1, 2, \ldots n \quad \text{(S6)}$$

In eq S6, t is the time, z is the distance along the adsorber, ρ is the framework density, ε is the bed voidage, v is the interstitial gas velocity, and $\bar{q}_i(t, z)$ is the *spatially averaged* molar loading within the crystallites of radius r_c, monitored at position z, and at time t. At the time, $t = 0$, the inlet to the adsorber, $z = 0$, is subjected to a step input of the n-component gas mixture, and this step input is maintained until the end of the adsorption cycle when steady-state conditions are reached.

$$t \geq 0;\ p_i(0, t) = p_{i0};\ u(0, t) = u_0 \quad \text{(S7)}$$

The *interstitial* gas velocity is related to the *superficial* gas velocity by

$$v = \frac{u}{\varepsilon} \quad \text{(S8)}$$

where $u_0 = v\varepsilon$ is the superficial gas velocity at the inlet to the adsorber. The superficial gas velocity is calculated from the flow rate of the gas mixture entering the breakthrough tube in the experiments.

The radial distribution of molar loadings, q_i, within a ZIF-8 crystallite, of radius r_c, is obtained from a solution of a set of differential equations describing the uptake

$$\rho \frac{\partial q_i(r, t)}{\partial t} = -\frac{1}{r^2}\frac{\partial}{\partial r}(r^2 N_i) \quad \text{(S9)}$$

The intracrystalline fluxes N_i in eq S9 are related to gradients in the chemical potentials by the Maxwell-Stefan (M-S) diffusion formulation[9−11]

$$N_i = -\rho Đ_i \frac{q_i}{RT}\frac{\partial \mu_i}{\partial r};\ i = 1, 2, \ldots n \quad \text{(S10)}$$

In eqs S9 and S10, R is the gas constant, T is the temperature, ρ represents the framework density of the microporous crystalline material, r is the radial distance coordinate, and the component loadings q_i are defined in terms of moles per kilogram of framework. The $Đ_i$ characterize and quantify the interaction between species i and pore walls. The M-S diffusivity $Đ_i$ equals the corresponding diffusivity for a unary system, determined at the same pore occupancy.[12] Furthermore, the M-S diffusivity $Đ_i$ for any species i in a mixture remains invariant to the choice of the partner(s) species.[12]

Extensive data from MD simulations for several guest/host combinations have established that the M-S diffusivities are generally dependent on the fractional occupancy $\theta = \frac{q}{q_{\text{sat}}}$.[12,13] The simplest model to describe this occupancy dependence is

$$Đ_i = Đ_i(0)(1 - \theta) \quad \text{(S11)}$$

where $Đ_1(0)$ is the M-S diffusivity at "zero-loading". Equation S11 is essentially based on a simple hopping model in which a molecule can jump from one adsorption site to an adjacent one, provided it is not already occupied. For the simulations of 50/50 $C_3H_6(1)/C_3H_8(2)$ mixture breakthroughs in fixed beds packed with ZIF-8 we use the following estimates of the M-S diffusivities at zero-loadings $Đ_1(0) = 1 \times 10^{-11}$ m^2 s^{-1}, $Đ_1(0)/Đ_2(0) = 100$. The chosen values are guided by the experimental data on transient unary uptakes in this work; see Figure 3 of the manuscript. These values are also in broad agreement with earlier Maxwell−Stefan analyses of diffusion of $C_3H_6(1)/C_3H_8(2)$ mixtures in ZIF-8.[3,4,14,15]

At thermodynamic equilibrium, the chemical potential of component i in the bulk fluid mixture equals the chemical potential of that component in the adsorbed phase. For the bulk fluid phase mixture, we have

$$\frac{1}{RT}\frac{\partial \mu_i}{\partial r} = \frac{\partial \ln p_i}{\partial r} = \frac{1}{p_i}\frac{\partial p_i}{\partial r};\ i = 1, 2, \ldots n \quad \text{(S12)}$$

In eq S12, p_i represents the partial pressure in the bulk fluid phase mixture. The chemical potential gradients $\frac{\partial \mu_i}{\partial r}$ can be related to the gradients of the molar loadings, q_i, by defining thermodynamic correction factors Γ_{ij}

$$\frac{q_i}{RT}\frac{\partial \mu_i}{\partial r} = \sum_{j=1}^{n} \Gamma_{ij}\frac{\partial q_j}{\partial r};\ \Gamma_{ij} = \frac{q_i}{f_i}\frac{\partial f_i}{\partial q_j};\ i, j = 1, \cdots n \quad \text{(S13)}$$

The thermodynamic correction factor Γ_{ij} can be calculated by differentiation of the model describing mixture adsorption equilibrium. In our simulations, the Ideal Adsorbed Solution Theory (IAST) of Myers and Prausnitz[16] is used for the determination of mixture adsorption equilibrium. For the IAST calculations, the experimental data on the unary isotherms of C_3H_6 and C_3H_8 in ZIF-8, as presented in Figure 2 of the article, were fitted with the Langmuir−Freundlich isotherm model.

At any time, t, during the transient approach to thermodynamic equilibrium, the spatial-averaged component loading within the crystallites of radius r_c is calculated using

$$\bar{q}_i(t) = \frac{3}{r_c^3}\int_0^{r_c} q_i(r, t) r^2 dr \quad \text{(S14)}$$

Summing eq S14 over all n species in the mixture allows calculation of the *total average* molar loading of the mixture within a ZIF-8 crystallite.

$$\bar{q}_t(t, z) = \sum_{i=1}^{n} \bar{q}_i(t, z) \quad \text{(S15)}$$

The term $\frac{\partial \bar{q}_i(t,z)}{\partial t}$ in eq S6 is determined by solving the set of eqs S9, S10, S14, and S15. At any time t, and position z, the component loadings at the outer surface of the particle $q_i(r_c, t, z)$ is in equilibrium with the bulk phase gas mixture with partial pressures $p_i(t, z)$ in the bulk gas mixture. The component loadings at the surface of the crystallites $q_i(r_c, t, z)$ are calculated using the IAST.

Further details of the numerical procedures used in solving the partial differential equations, are provided by Krishna and co-workers.[6,7,17,18]

https://doi.org/10.1021/acsnano.3c11385
ACS Nano 2024, 18, 3614−3626

COMSOL MULTIPHYSICS SIMULATION

We established a simple three-dimensional fixed bed mass transfer model using COMSOL Multiphysics to discuss the mass transfer laws of ZIF-8 under different flow rates and intracrystalline diffusion conditions at constant temperature and without interaction between components (Figure 6). And based on the experiment, the breakthrough equilibrium condition is determined by the outlet concentration (C/C_0 of both components is greater than 0.975). All physical fields and related nodes in the model are constructed by using the existing components of COMSOL Multiphysics without any special assumptions. The basic parameter settings are listed in Table S5. Below is an explanation of the physical fields and main nodes used in the model:

1. The Laminar Flow Interface (spf). This physical field is used to solve the Navier−Stokes equation for momentum conservation and the continuity equation for mass conservation. The gas mixture follows the incompressible flow, and its basic assumption equation can be expressed as

$$\rho(\mathbf{u}\cdot\nabla)\mathbf{u} = \nabla\cdot[-p\mathbf{I} + \mathbf{K}] + \mathbf{F} \tag{S16}$$

$$\rho\nabla\cdot\mathbf{u} = 0 \tag{S17}$$

$$\mathbf{K} = \mu(\nabla\mathbf{u} + (\nabla\mathbf{u})^{\mathrm{T}}) \tag{S18}$$

Where, ρ is the fluid density, μ is the dynamic viscosity of the fluid, $\mathbf{u}$ is the velocity vector, p is the pressure, $\mathbf{K}$ is the viscous stress tensor, $\mathbf{F}$ is the external force acting on the fluid, and $\mathbf{I}$ is the identity matrix.

For the initial and boundary conditions, the initial values of the velocity vector and pressure are set to 0, indicating that the mixture has not yet begun to flow in. The wall condition is set to no slip, where $\mathbf{u} = 0$. For the inlet and outlet conditions, generally speaking, setting the velocity vector at both the inlet and outlet may lead to difficulty in convergence. Therefore, we set the pressure boundary condition at the inlet with a static pressure of 10^5 Pa, a normal flow direction, and suppressed backflow. The basic equation here can be expressed as

$$\mathbf{n}^{\mathrm{T}}[-p\mathbf{I} + \mathbf{K}]\mathbf{n} = -\widehat{p_0} \tag{S19}$$

$$\widehat{p_0} \geq p_0,\ \mathbf{u}\cdot\mathbf{t} = 0 \tag{S20}$$

Where, $\mathbf{t}$ is the tangent vector, $\mathbf{n}$ is the normal vector, and p_0 is the static pressure.

The outlet is set as a velocity boundary condition, and the velocity is limited to the normal outflow velocity; then, the velocity vector here can be expressed as

$$\mathbf{u} = U_0\mathbf{n} \tag{S21}$$

Where, U_0 is the mixture flow rate (linear velocity).

In particular, we used the porous media domains to represent the fixed bed region filled with adsorbent particles. If the characteristics of the fluid and porous matrix are defined, according to Brinkman Equations Theory,[19,20] the basic equation for the adsorbent region can be further rewritten as

$$\frac{1}{\varepsilon_{\mathrm{p}}}\rho(\mathbf{u}\cdot\nabla)\mathbf{u}\frac{1}{\varepsilon_{\mathrm{p}}} = \nabla\cdot[-p\mathbf{I} + \mathbf{K}] - \left(\mu\kappa^{-1} + \beta\rho|\mathbf{u}| + \frac{Q_{\mathrm{m}}}{\varepsilon_{\mathrm{p}}^{\,2}}\right)\mathbf{u} + \mathbf{F} \tag{S22}$$

$$\rho\nabla\cdot\mathbf{u} = Q_{\mathrm{m}} \tag{S23}$$

$$\mathbf{K} = \mu\frac{1}{\varepsilon_{\mathrm{p}}}(\nabla\mathbf{u} + (\nabla\mathbf{u})^{\mathrm{T}})) - \frac{2}{3}\mu\frac{1}{\varepsilon_{\mathrm{p}}}(\nabla\cdot\mathbf{u})\mathbf{I} \tag{S24}$$

Where, ε_{p} is the porosity; Q_m is the mass source, which is used to explain mass deposition and creation within the operational range (assuming mass exchange occurs under zero velocity conditions). κ is the permeability of porous media; β Is the slip length.

For the definition of porous media permeability, due to significant differences in particle sizes among different ZIF-8 in our work, the Kozeny Carman model[21,22] associated with particle size was selected. In this model, κ can be expressed as

$$\kappa = \frac{d_p^2}{180}\frac{\varepsilon_{\mathrm{p}}^{\,3}}{(1-\varepsilon_{\mathrm{p}})^2} \tag{S25}$$

Where, d_p is the particle size of the adsorbent.

2. The Transport of Diluted Species Interface (tds). This physical field is used to calculate the concentration field of the diluted substances. The driving force of mass transfer is described by Fick's law, and the basic equation can be expressed as

$$\frac{\partial c_i}{\partial t} + \nabla\cdot\mathbf{J_i} + \mathbf{u}\cdot\nabla c_i = R_i \tag{S26}$$

$$\mathbf{J_i} = -D_i\nabla c_i \tag{S27}$$

Where, R_i is the mass transfer rate of the component (corresponding to the reaction occurring in the pore space outside the adsorbent particles), c_i represents the interstitial concentration of the component (the physical concentration of the fluid per unit volume flowing between adsorbent particles), $\mathbf{J_i}$ is the diffusion flux of the component, D_i is the diffusion coefficient of the component, and $\mathbf{u}\cdot\nabla c_i$ represents the convective term caused by the velocity field.

The "porous medium" node is selected to simulate the concentration of diluted substances transported by the fluid phase through the pores of solid porous medium so as to obtain the mass transfer in the gaps between particles. The basic equation within the adsorbent region can be rewritten as

$$\frac{\partial(\varepsilon_p c_i)}{\partial t} + \frac{\partial(\rho c_{p,i})}{\partial t} + \nabla\cdot\mathbf{J_i} + \mathbf{u}\cdot\nabla c_i = R_i + S_i \tag{S28}$$

$$\mathbf{J_i} = -(D_{D,i} + D_{e,i})\nabla c_i \tag{S29}$$

$$D_{e,i} = \frac{\varepsilon_p}{\tau_{F,i}}D_{F,i} \tag{S30}$$

Where, R_i is the reaction rate (which can represent the reaction between the gas phase and solid phase); S_i is an arbitrary source term that represents the increase/decrease in material within the region caused by fluid flow; ε_p is the material filling porosity of the fixed bed column; $c_{p,i}$ represents the component concentration adsorbed by absorbent; $D_{D,i}$ is the diffusion tensor; $D_{e,i}$ is the effective diffusion coefficient; $D_{F,i}$ is the fluid diffusion coefficient of each component, and in order to maintain consistency, universal values (default value) of 10^{-9} m^2/s are selected for all components; $\tau_{F,i}$ is the tortuosity, following the Millington Quirk model,[5] which can be expressed as

$$\tau_{F,i} = \varepsilon_p^{\,-1/3} \tag{S31}$$

https://doi.org/10.1021/acsnano.3c11385
ACS Nano 2024, 18, 3614−3626

We add the "reaction particle bed" node to represent the diffusion of gas within the absorbent. From the perspective of the fluid within the absorbent, the rate of decrease in free gas concentration caused by absorbent adsorption can be expressed as

$$\varepsilon_{pe}\frac{\partial c_{pe,i}}{\partial t} + \frac{1}{r^2 {r_{pe}}^2}\frac{\partial}{\partial r}\left(-r^2 D_{pe,i}\frac{c_{pe,i}}{\partial r}\right) = R_{pe,i} \tag{S32}$$

Where, $R_{pe,i}$ is the adsorption rate of the adsorbent on component i. $R_{pe,i}$ is set as a conditional function. When $c_{pe,i} > 0$, the reaction rate follows the negative number of the adsorption rate-adsorption capacity interpolation function $(V_i\ (c_i))$ (see next part for details), otherwise it is 0; $c_{pe,i}$ is the concentration of component i in the absorbent pores.

For adsorbent particles, we assume that they are uniformly distributed spheres of the same size, with corresponding radii and porosities of r_{pe} and ε_{pe}, respectively. And we assume that the concentration change only occurs in the radial direction of the adsorbent sphere and is independent of the space angle's direction. So, the dimensionless particle radius can be defined, and the basic equation is

$$r = \frac{r_{dim}}{r_{pe}},\ 0 \le r \le 1 \tag{S33}$$

Where, r_{dim} is the radial coordinate in the spherical particle, r_{pe} is the particle radius.

So, the diffusion flux of spherical particles J_{pe} can be expressed as

$$J_{pe}: (c_{pe,i})_{r=1} = c_i,\ \frac{1}{r_{pe}}\left(D_{pe,i}\frac{\partial c_{pe,i}}{\partial r}\right)_{r=1} = J_{pe} \tag{S34}$$

$$R_i = J_{pe}(1-\varepsilon_{pe})\frac{A_{pe}}{V_{pe}} \tag{S35}$$

Where, V_{pe} and A_{pe} refer to the volume and outer surface of the absorbent particles, respectively.

For the absorbent particle-fluid surface, it is coupled in a continuous concentration manner (assuming that there is no mass transfer resistance on the side of the fluid, the concentration in the fluid is equal to the concentration in the particle surface pores), which means that

$$c_{pe,i} = c_i \tag{S36}$$

In other aspects, the adsorbent particles are dispersed in cube root mode (default mode), and the number of units is set to 10 (default value).

Finally, the diffusion of gas within the adsorbent particles also follows the Millington Quirk model, whose basic equation is

$$D_{peff,i} = {\varepsilon_{pe}}^{4/3} D_{pe,i} \tag{S37}$$

Where, $D_{peff,i}$ is the effective diffusion coefficient; $D_{pe,i}$ is the diffusion coefficient of the component within the absorbent particle. But for our work, the difference in the adsorption rate of sizes absorbents is uniformly attributed to the adsorption rate-adsorption capacity interpolation function $(V_i\ (c_i))$, which replaces the role of intracrystalline diffusion coefficient. Therefore, it is set at 10^{-9} m^2/s, which is consistent with the diffusion outside the absorbent particle (it can also be set to other values).

3. Domain ODEs and DAEs (dode). Previous work generally believed that the adsorption rate/adsorption driving force of the material was determined by the loading amount/chemical potential, and the Linear Driving Force (LDF) model, or other similar forms, was usually used to calculate the adsorption rate of the adsorbent.[24−26] However, in this work, due to the rapid gas diffusion, there is a significant deviation in the diffusion coefficient obtained from the kinetic adsorption test of small particle ZIF-8 (Table S2), and the adsorption driving force based on the diffusion coefficient will also have a significant deviation. To this end, we fitted and directly transformed the kinetic data of different ZIF-8 under breakthrough partial pressure into an interpolation function of adsorption rate-adsorption capacity (Figure 6c,d), which serves as the basis for determining the adsorbent's adsorption rate, thus avoiding the conversion of diffusion coefficients. For this purpose, this physical field was added to achieve the interpolation function representation of the adsorption rate.

The function of this physical field is to add equations unrelated to space to the domain, mainly used to represent the adsorption rate of the absorbent on different components. The basic equations are

$$f = d_a\frac{\partial \mathbf{u}}{\partial t} \tag{S38}$$

$$\mathbf{u} = [c_1,\ c_2]^T \tag{S39}$$

Where, $\mathbf{u}$ is the concentration matrix of different components; f is the adsorption rate, which is set as a conditional function. When $c_i > 0$, the reaction rate follows the adsorption rate-adsorption capacity interpolation function $(V_i\ (c_i))$, otherwise it is 0. d_a is the quality coefficient, which is $\begin{bmatrix}1 & 0\\ 0 & 1\end{bmatrix}$. The initial reaction rate and initial concentration are both set to 0.

4. Reacting Flow, Diluted Species Multiphysics (rfd). This multiphysics is used to simulate mass transfer and reaction in gas or liquid, synchronizing the characteristics of single-phase flow, interface, and dilute substance transport interface. After adding, the velocity field used by the dilute substance transport interface is synchronized with the velocity field calculated in the fluid flow interface. On the coupling interface setting, fluid flow is represented by the "Laminar Flow (spf)" physical field, and dilute substance transfer is represented by the "Transport of Diluted Species (tds)" physical field.

5. Calculation Examples. In order to better understand the model, we selected the calculation results of ZIF-8-9 μm mentioned in the main text at 0.01 and 0.001m/s for further analysis (Figures S14−S15). And at each flow rate condition, we selected four intermediate moments to explain the adsorption process of different components.

Under high flow rate conditions (0.01 m/s), we can see that the material exhibits the preferential adsorption of propylene at any time before equilibrium. Therefore, for gas that has not been adsorbed (gas concentration at the outlet), the concentration of propylene has always been lower than that of propane. However, as the adsorption proceeds, the results of the adsorption amount become closer to the static adsorption results, resulting in a smaller propylene/propane adsorption amount ratio.

The calculation results under low flow rate (0.001 m/s) conditions are relatively complex. For ease of understanding, we use blue to indicate the part that prioritizes the absorption of propane and green to indicate the part that prioritizes the absorption of propylene. In the initial stage of adsorption (1500

https://doi.org/10.1021/acsnano.3c11385
ACS Nano 2024, 18, 3614−3626

s), due to the high adsorption rate of propylene, the material overall exhibits the property of preferentially adsorbing propylene. But in other aspects, due to the slow adsorption of propane, more unadsorbed propane reaches the rear end (outlet) of the fixed bed column earlier. Therefore, for the material at the outlet, it will start adsorbing propane before propylene and will be displayed in blue at the outlet. As the propylene begins to reach the outlet, the corresponding blue part begins to disappear (2400 s). In the next stage (3300 s), due to the earlier start of adsorption by the material at the inlet, the static adsorption results are achieved faster, exhibiting a preference for propane adsorption, while the material at the outlet still exhibits dynamic adsorption results. In the final stage (4200 s), the material as a whole exhibits a static adsorption result.

ASSOCIATED CONTENT

Supporting Information

The Supporting Information is available free of charge at https://pubs.acs.org/doi/10.1021/acsnano.3c11385.

Figures S1−S16 and Tables S1−S5 show the three-dimensional molecular sizes of propane and propylene, the SEM images, the BET surface area results, the adsorption isotherms, the kinetic uptake plots, the fitting results of diffusion time constant, the breakthrough experiment results, the discretization scheme and model diagram in transient breakthrough simulation, the breakthrough calculation results in COMSOL Multiphysics simulation, the thermogravimetric analysis results, the saturated adsorption capacity, Kinetic selectivity, diffusion time constant and results, the main parameters set in COMSOL Multiphysics simulation (PDF)

Video animations of the breakthrough simulation of ZIF-8-9 μm presented in Figure 3a (MP4)

Video animations of the breakthrough simulation of ZIF-8-72 μm presented in Figure 3a (MP4)

Video animations of the breakthrough simulation of ZIF-8-141 μm presented in Figure 3a (MP4)

Video animations of the breakthrough simulation of ZIF-8-224 μm presented in Figure 3a (MP4)

AUTHOR INFORMATION

Corresponding Authors

Zongbi Bao − *Key Laboratory of Biomass Chemical Engineering of Ministry of Education, College of Chemical and Biological Engineering, Zhejiang University, Hangzhou 310027, P.R. China; Institute of Zhejiang University-Quzhou, Quzhou 324000, P.R. China;* orcid.org/0000-0003-4327-3028; Email: baozb@zju.edu.cn

Fang Zheng − *Institute of Zhejiang University-Quzhou, Quzhou 324000, P.R. China;* orcid.org/0000-0001-9628-5706; Email: zhengfang_@zju.edu.cn

Rajamani Krishna − *Van 't Hoff Institute for Molecular Sciences, University of Amsterdam, 1098 XH Amsterdam, The Netherlands;* orcid.org/0000-0002-4784-8530; Email: r.krishna@contact.uva.nl

Authors

Linghe Yang − *Key Laboratory of Biomass Chemical Engineering of Ministry of Education, College of Chemical and Biological Engineering, Zhejiang University, Hangzhou 310027, P.R. China*

Ying Liu − *Key Laboratory of Biomass Chemical Engineering of Ministry of Education, College of Chemical and Biological Engineering, Zhejiang University, Hangzhou 310027, P.R. China*

Fuxing Shen − *Institute of Zhejiang University-Quzhou, Quzhou 324000, P.R. China*

Baojian Liu − *Institute of Zhejiang University-Quzhou, Quzhou 324000, P.R. China*

Zhiguo Zhang − *Key Laboratory of Biomass Chemical Engineering of Ministry of Education, College of Chemical and Biological Engineering, Zhejiang University, Hangzhou 310027, P.R. China; Institute of Zhejiang University-Quzhou, Quzhou 324000, P.R. China;* orcid.org/0000-0003-1681-4853

Qiwei Yang − *Key Laboratory of Biomass Chemical Engineering of Ministry of Education, College of Chemical and Biological Engineering, Zhejiang University, Hangzhou 310027, P.R. China; Institute of Zhejiang University-Quzhou, Quzhou 324000, P.R. China*

Qilong Ren − *Key Laboratory of Biomass Chemical Engineering of Ministry of Education, College of Chemical and Biological Engineering, Zhejiang University, Hangzhou 310027, P.R. China; Institute of Zhejiang University-Quzhou, Quzhou 324000, P.R. China*

Complete contact information is available at: https://pubs.acs.org/10.1021/acsnano.3c11385

Author Contributions

$^{\perp}$L.Y. and Y.L. contributed equally to this work and should be considered cofirst authors.

Notes

The authors declare no competing financial interest.

ACKNOWLEDGMENTS

We are grateful for the financial support by the National Natural Science Foundation of China (No. 22225802, No. 22288102, No. 22141001) and Zhejiang Provincial Natural Science Foundation of China (No. LZ22B060002).

LATIN ALPHABET

c_i: molar concentration of species i, mol m^{-3}
c_t: total molar concentration in mixture, mol m^{-3}
c_{i0}: molar concentration of species i in fluid mixture at inlet to adsorber, mol m^{-3}
$Đ_i$: Maxwell-Stefan diffusivity for molecule-wall interaction, m^2 s^{-1}
n: number of species in the mixture, dimensionless
L: length of packed bed adsorber, m
N_i: molar flux of species i with respect to framework, mol m^{-2} s^{-1}
p_i: partial pressure of species i in mixture, Pa
p_t: total system pressure, Pa
q_i: component molar loading of species i, mol kg^{-1}
q_t: total molar loading in mixture, mol kg^{-1}
$\overline{q}_i(t)$: radial-averaged component loading of species i, mol kg^{-1}
r: radial direction coordinate, m
r_c: radius of crystallite, m
R: gas constant, 8.314 J mol^{-1} K^{-1}
t: time, s
T: absolute temperature, K
u: superficial gas velocity in packed bed, m s^{-1}

https://doi.org/10.1021/acsnano.3c11385
ACS Nano 2024, 18, 3614−3626

v: interstitial gas velocity in packed bed, m s^{-1}
z: distance along the adsorber, m

GREEK ALPHABET

Γ_{ij}: thermodynamic correction factors, dimensionless
ε: voidage of packed bed, dimensionless
ρ: framework density, kg m^{-3}

SUBSCRIPTS

i: referring to component i
t: referring to total mixture

REFERENCES

(1) Akah, A.; Al-Ghrami, M. Maximizing propylene production via FCC technology. *Appl. Petrochem. Res.* **2015**, *5*, 377−392.
(2) Lavrenov, A.; Saifulina, L.; Buluchevskii, E.; Bogdanets, E. Propylene production technology: Today and tomorrow. *Catal. Ind.* **2015**, *7*, 175−187.
(3) Phung, T. K.; Pham, T. L. M.; Vu, K. B.; Busca, G. (Bio) Propylene production processes: A critical review. *J. Environ. Chem. Eng.* **2021**, *9* (4), 105673.
(4) van Miltenburg, A.; Gascon, J.; Zhu, W.; Kapteijn, F.; Moulijn, J. A. Propylene/propane mixture adsorption on faujasite sorbents. *Adsorption* **2008**, *14*, 309−321.
(5) Li, J.-R.; Kuppler, R. J.; Zhou, H.-C. Selective gas adsorption and separation in metal-organic frameworks. *Chem. Soc. Rev.* **2009**, *38* (5), 1477−1504.
(6) Plaza, M.; Ferreira, A.; Santos, J.; Ribeiro, A.; Müller, U.; Trukhan, N.; Loureiro, J.; Rodrigues, A. Propane/propylene separation by adsorption using shaped copper trimesate MOF. *Microporous Mesoporous Mater.* **2012**, *157*, 101−111.
(7) Cavalcante, C. Industrial adsorption separation processes: Fundamentals, modeling and applications. *Lat. Am. Appl. Res.* **2000**, *30* (4), 357−364.
(8) Farmahini, A. H.; Krishnamurthy, S.; Friedrich, D.; Brandani, S.; Sarkisov, L. From crystal to adsorption column: challenges in multiscale computational screening of materials for adsorption separation processes. *Ind. Eng. Chem. Res.* **2018**, *57* (45), 15491−15511.
(9) Nikolić, D. D.; Kikkinides, E. S. Modelling and optimization of hybrid PSA/membrane separation processes. *Adsorption* **2015**, *21*, 283−305.
(10) Rasouli, M.; Yaghobi, N.; Allahgholipour, F.; Atashi, H. Para-xylene adsorption separation process using nano-zeolite Ba-X. *Chem. Eng. Res. Des.* **2014**, *92* (6), 1192−1199.
(11) Belmabkhout, Y.; Bhatt, P. M.; Adil, K.; Pillai, R. S.; Cadiau, A.; Shkurenko, A.; Maurin, G.; Liu, G.; Koros, W. J.; Eddaoudi, M. Natural gas upgrading using a fluorinated MOF with tuned H2S and CO_2 adsorption selectivity. *Nat. Energy* **2018**, *3* (12), 1059−1066.
(12) Boyd, P. G.; Chidambaram, A.; García-Díez, E.; Ireland, C. P.; Daff, T. D.; Bounds, R.; Gładysiak, A.; Schouwink, P.; Moosavi, S. M.; Maroto-Valer, M. M.; et al. Data-driven design of metal-organic frameworks for wet flue gas CO2 capture. *Nature* **2019**, *576* (7786), 253−256.
(13) Datta, S. J.; Mayoral, A.; Murthy Srivatsa Bettahalli, N.; Bhatt, P. M.; Karunakaran, M.; Carja, I. D.; Fan, D.; Graziane M. Mileo, P.; Semino, R.; Maurin, G.; et al. Rational design of mixed-matrix metal-organic framework membranes for molecular separations. *Science* **2022**, *376* (6597), 1080−1087.
(14) Ding, Q.; Zhang, Z.; Yu, C.; Zhang, P.; Wang, J.; Cui, X.; He, C.-H.; Deng, S.; Xing, H. Exploiting equilibrium-kinetic synergetic effect for separation of ethylene and ethane in a microporous metal-organic framework. *Sci. Adv.* **2020**, *6* (15), eaaz4322.
(15) Li, L.; Guo, L.; Olson, D. H.; Xian, S.; Zhang, Z.; Yang, Q.; Wu, K.; Yang, Y.; Bao, Z.; Ren, Q.; Li, J. Discrimination of xylene isomers in a stacked coordination polymer. *Science* **2022**, *377* (6603), 335−339.
(16) Li, L.; Lin, R.-B.; Krishna, R.; Li, H.; Xiang, S.; Wu, H.; Li, J.; Zhou, W.; Chen, B. Ethane/ethylene separation in a metal-organic framework with iron-peroxo sites. *Science* **2018**, *362* (6413), 443−446.
(17) Wang, H.; Dong, X.; Lin, J.; Teat, S. J.; Jensen, S.; Cure, J.; Alexandrov, E. V.; Xia, Q.; Tan, K.; Wang, Q.; et al. Topologically guided tuning of Zr-MOF pore structures for highly selective separation of C6 alkane isomers. *Nat. Commun.* **2018**, *9* (1), 1745.
(18) Zeng, H.; Xie, M.; Wang, T.; Wei, R.-J.; Xie, X.-J.; Zhao, Y.; Lu, W.; Li, D. Orthogonal-array dynamic molecular sieving of propylene/propane mixtures. *Nature* **2021**, *595* (7868), 542−548.
(19) Abedini, H.; Asgari, M.; Watt Coull, M.; Shariati, A.; Reza Khosravi-Nikou, M. Efficient production of polymer-grade propylene from the propane/propylene binary mixture using Cu-MOF-74 framework. *Sep. Purif. Technol.* **2021**, *276*, 119172.
(20) Bae, Y. S.; Lee, C. Y.; Kim, K. C.; Farha, O. K.; Nickias, P.; Hupp, J. T.; Nguyen, S. T.; Snurr, R. Q. High propene/propane selectivity in isostructural metal-organic frameworks with high densities of open metal sites. *Angew. Chem.* **2012**, *124* (8), 1893−1896.
(21) Bloch, E. D.; Queen, W. L.; Krishna, R.; Zadrozny, J. M.; Brown, C. M.; Long, J. R. Hydrocarbon separations in a metal-organic framework with open iron (II) coordination sites. *science* **2012**, *335* (6076), 1606−1610.
(22) Jiang, S.; Li, J.; Feng, M.; Chen, R.; Guo, L.; Xu, Q.; Chen, L.; Shen, F.; Zhang, Z.; Yang, Y.; et al. Hydrophobic paraffin-selective pillared-layer MOFs for olefin purification. *J. Mater. Chem. A* **2022**, *10* (45), 24127−24136.
(23) Khalighi, M.; Chen, Y.; Farooq, S.; Karimi, I.; Jiang, J. Propylene/propane separation using SiCHA. *Ind. Eng. Chem. Res.* **2013**, *52* (10), 3877−3892.
(24) Li, L.; Lin, R.-B.; Wang, X.; Zhou, W.; Jia, L.; Li, J.; Chen, B. Kinetic separation of propylene over propane in a microporous metal-organic framework. *Chem. Eng. J.* **2018**, *354*, 977−982.
(25) Palomino, M.; Cantín, A.; Corma, A.; Leiva, S.; Rey, F.; Valencia, S. Pure silica ITQ-32 zeolite allows separation of linear olefins from paraffins. *Chem. Commun.* **2007**, No. 12, 1233−1235.
(26) Selzer, C.; Werner, A.; Kaskel, S. Selective adsorption of propene over propane on hierarchical zeolite ZSM-58. *Ind. Eng. Chem. Res.* **2018**, *57* (19), 6609−6617.
(27) Chen, Y.; Qiao, Z.; Lv, D.; Duan, C.; Sun, X.; Wu, H.; Shi, R.; Xia, Q.; Li, Z. Efficient adsorptive separation of C_3H_6 over C_3H_8 on flexible and thermoresponsive CPL-1. *Chem. Eng. J.* **2017**, *328*, 360−367.
(28) Wang, X.; Krishna, R.; Li, L.; Wang, B.; He, T.; Zhang, Y.-Z.; Li, J.-R.; Li, J. Guest-dependent pressure induced gate-opening effect enables effective separation of propene and propane in a flexible MOF. *Chem. Eng. J.* **2018**, *346*, 489−496.
(29) Cadiau, A.; Adil, K.; Bhatt, P.; Belmabkhout, Y.; Eddaoudi, M. A metal-organic framework-based splitter for separating propylene from propane. *Science* **2016**, *353* (6295), 137−140.
(30) Wang, H.; Dong, X.; Colombo, V.; Wang, Q.; Liu, Y.; Liu, W.; Wang, X. L.; Huang, X. Y.; Proserpio, D. M.; Sironi, A.; et al. Tailor made microporous metal-organic frameworks for the full separation of propane from propylene through selective size exclusion. *Adv. Mater.* **2018**, *30* (49), 1805088.
(31) Li, X.; Wang, H.; Zou, J.; Li, J. Metal-organic frameworks with ftw-type connectivity: design, pore structure engineering, and potential applications. *CrystEngComm* **2022**, *24* (12), 2189−2200.
(32) Lin, R.-B.; Zhang, Z.; Chen, B. Achieving high performance metal-organic framework materials through pore engineering. *Acc. Chem. Res.* **2021**, *54* (17), 3362−3376.
(33) Krishna, R. Synergistic and antisynergistic intracrystalline diffusional influences on mixture separations in fixed-bed adsorbers. *Precis. Chem.* **2023**, *1* (2), 83−93.
(34) Yang, J.; Krishna, R.; Li, J.; Li, J. Experiments and simulations on separating a CO_2/CH_4 mixture using K-KFI at low and high pressures. *Microporous Mesoporous Mater.* **2014**, *184*, 21.
(35) Dong, X.; Lin, Y. Synthesis of an organophilic ZIF-71 membrane for pervaporation solvent separation. *Chem. Commun.* **2013**, *49* (12), 1196−1198.

https://doi.org/10.1021/acsnano.3c11385
ACS Nano 2024, 18, 3614−3626

(36) Hartmann, M.; Böhme, U.; Hovestadt, M.; Paula, C. Adsorptive separation of olefin/paraffin mixtures with ZIF-4. *Langmuir* **2015**, *31* (45), 12382−12389.
(37) Li, Y.; Liang, F.; Bux, H.; Yang, W.; Caro, J. Zeolitic imidazolate framework ZIF-7 based molecular sieve membrane for hydrogen separation. *J. Membr. Sci.* **2010**, *354* (1−2), 48−54.
(38) Liu, Y.; Hu, E.; Khan, E. A.; Lai, Z. Synthesis and characterization of ZIF-69 membranes and separation for CO_2/CO mixture. *J. Membr. Sci.* **2010**, *353* (1−2), 36−40.
(39) Mubashir, M.; Dumée, L. F.; Fong, Y. Y.; Jusoh, N.; Lukose, J.; Chai, W. S.; Show, P. L. Cellulose acetate-based membranes by interfacial engineering and integration of ZIF-62 glass nanoparticles for CO2 separation. *J. Hazard. Mater.* **2021**, *415*, 125639.
(40) Zhong, G.; Liu, D.; Zhang, J. The application of ZIF-67 and its derivatives: adsorption, separation, electrochemistry and catalysts. *J. Mater. Chem. A* **2018**, *6* (5), 1887−1899.
(41) Bux, H.; Chmelik, C.; Krishna, R.; Caro, J. Ethene/ethane separation by the MOF membrane ZIF-8: Molecular correlation of permeation, adsorption, diffusion. *J. Membr. Sci.* **2011**, *369* (1−2), 284−289.
(42) Jameh, A. A.; Mohammadi, T.; Bakhtiari, O.; Mahdyarfar, M. Synthesis and modification of Zeolitic Imidazolate Framework (ZIF-8) nanoparticles as highly efficient adsorbent for H2S and CO2 removal from natural gas. *J. Environ. Chem. Eng.* **2019**, *7* (3), 103058.
(43) Magdysyuk, O.; Adams, F.; Liermann, H.-P.; Spanopoulos, I.; Trikalitis, P.; Hirscher, M.; Morris, R.; Duncan, M.; McCormick, L.; Dinnebier, R. Understanding the adsorption mechanism of noble gases Kr and Xe in CPO-27-Ni, CPO-27-Mg, and ZIF-8. *Phys. Chem. Chem. Phys.* **2014**, *16* (43), 23908−23914.
(44) Mendes, P. A.; Rodrigues, A. E.; Horcajada, P.; Serre, C.; Silva, J. A. Single and multicomponent adsorption of hexane isomers in the microporous ZIF-8. *Microporous Mesoporous Mater.* **2014**, *194*, 146−156.
(45) Pan, Y.; Li, T.; Lestari, G.; Lai, Z. Effective separation of propylene/propane binary mixtures by ZIF-8 membranes. *J. Membr. Sci.* **2012**, *390*, 93−98.
(46) Zhang, K.; Lively, R. P.; Zhang, C.; Koros, W. J.; Chance, R. R. Investigating the intrinsic ethanol/water separation capability of ZIF-8: an adsorption and diffusion study. *J. Phys. Chem. C* **2013**, *117* (14), 7214−7225.
(47) Zhang, L.; Qian, G.; Liu, Z.; Cui, Q.; Wang, H.; Yao, H. Adsorption and separation properties of n-pentane/isopentane on ZIF-8. *Sep. Purif. Technol.* **2015**, *156*, 472−479.
(48) Böhme, U.; Barth, B.; Paula, C.; Kuhnt, A.; Schwieger, W.; Mundstock, A.; Caro, J. r.; Hartmann, M. Ethene/ethane and propene/propane separation via the olefin and paraffin selective metal-organic framework adsorbents CPO-27 and ZIF-8. *Langmuir* **2013**, *29* (27), 8592−8600.
(49) Do, D.; Do, H. Cooperative and competitive adsorption of ethylene, ethane, nitrogen and argon on graphitized carbon black and in slit pores. *Adsorption* **2005**, *11* (1), 35−50.
(50) Kroon, M. C.; Vega, L. F. Selective paraffin removal from ethane/ethylene mixtures by adsorption into aluminum methylphosphonate-α: a molecular simulation study. *Langmuir* **2009**, *25* (4), 2148−2152.
(51) Andres-Garcia, E.; Lopez-Cabrelles, J.; Oar-Arteta, L.; Roldan-Martinez, B.; Cano-Padilla, M.; Gascon, J.; Minguez Espallargas, G.; Kapteijn, F. Cation influence in adsorptive propane/propylene separation in ZIF-8 (SOD) topology. *Chem. Eng. J.* **2019**, *371*, 848−856.
(52) Böhme, U.; Paula, C.; Reddy Marthala, V.; Caro, J.; Hartmann, M. Exceptional Adsorption and Separation Properties of the Molecular Sieve ZIF 8. *Chem. Ing. Technol.* **2013**, *85* (11), 1707−1713.
(53) Li, K.; Olson, D. H.; Seidel, J.; Emge, T. J.; Gong, H.; Zeng, H.; Li, J. Zeolitic imidazolate frameworks for kinetic separation of propane and propene. *J. Am. Chem. Soc.* **2009**, *131* (30), 10368−10369.
(54) Zhang, C.; Lively, R. P.; Zhang, K.; Johnson, J. R.; Karvan, O.; Koros, W. J. Unexpected molecular sieving properties of zeolitic imidazolate framework-8. *journal of physical chemistry letters* **2012**, *3* (16), 2130−2134.
(55) Krishna, R.; Wesselingh, J. A. The Maxwell-Stefan approach to mass transfer. *Chem. Eng. Sci.* **1997**, *52* (6), 861−911.
(56) Krishna, R. The Maxwell-Stefan description of mixture diffusion in nanoporous crystalline materials. *Microporous Mesoporous Mater.* **2014**, *185*, 30−50.
(57) Krishna, R. Highlighting the influence of thermodynamic coupling on kinetic separations with microporous crystalline materials. *ACS Omega* **2019**, *4* (2), 3409−3419.
(58) Krishna, R.; Baur, R. Modelling issues in zeolite based separation processes. *Sep. Purif. Technol.* **2003**, *33* (3), 213−254.

https://doi.org/10.1021/acsnano.3c11385
ACS Nano 2024, 18, 3614−3626

Supporting Information

Leveraging Diffusion Kinetics to Reverse Propane/Propylene Adsorption in Zeolitic Imidazolate Framework-8

Linghe Yang,[†,§] Ying Liu,[†,§] Fang Zheng,[,‡], Fuxing Shen,[‡] Baojian Liu,[‡] Rajamani Krishna,[*,§] Zhiguo Zhang,[†,‡] Qiwei Yang,[†,‡] Qilong Ren,[†,‡] and Zongbi Bao*[†,‡]*

† Key Laboratory of Biomass Chemical Engineering of Ministry of Education, College of Chemical and Biological Engineering, Zhejiang University, Hangzhou 310027 (P.R. China)

‡ Institute of Zhejiang University-Quzhou, Quzhou 324000 (P.R. China)

§ Van 't Hoff Institute for Molecular Sciences, University of Amsterdam, Science Park 904, 1098 XH Amsterdam (The Netherlands)

Table of Contents

Supporting Figures and Tables

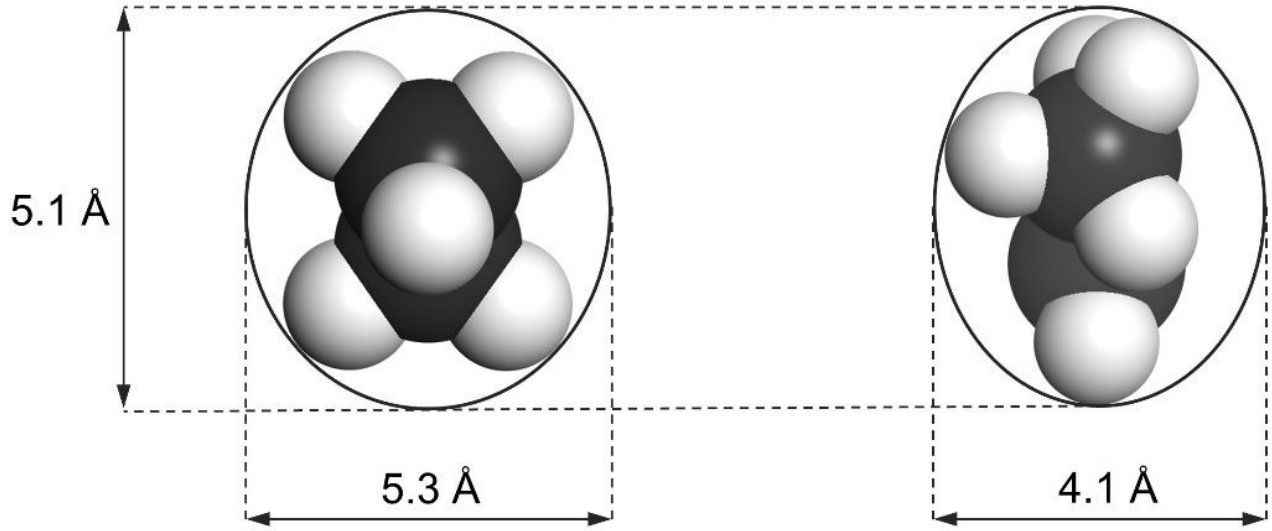

Figure S1. Three-dimensional molecular sizes of propane (left) and propylene (right).

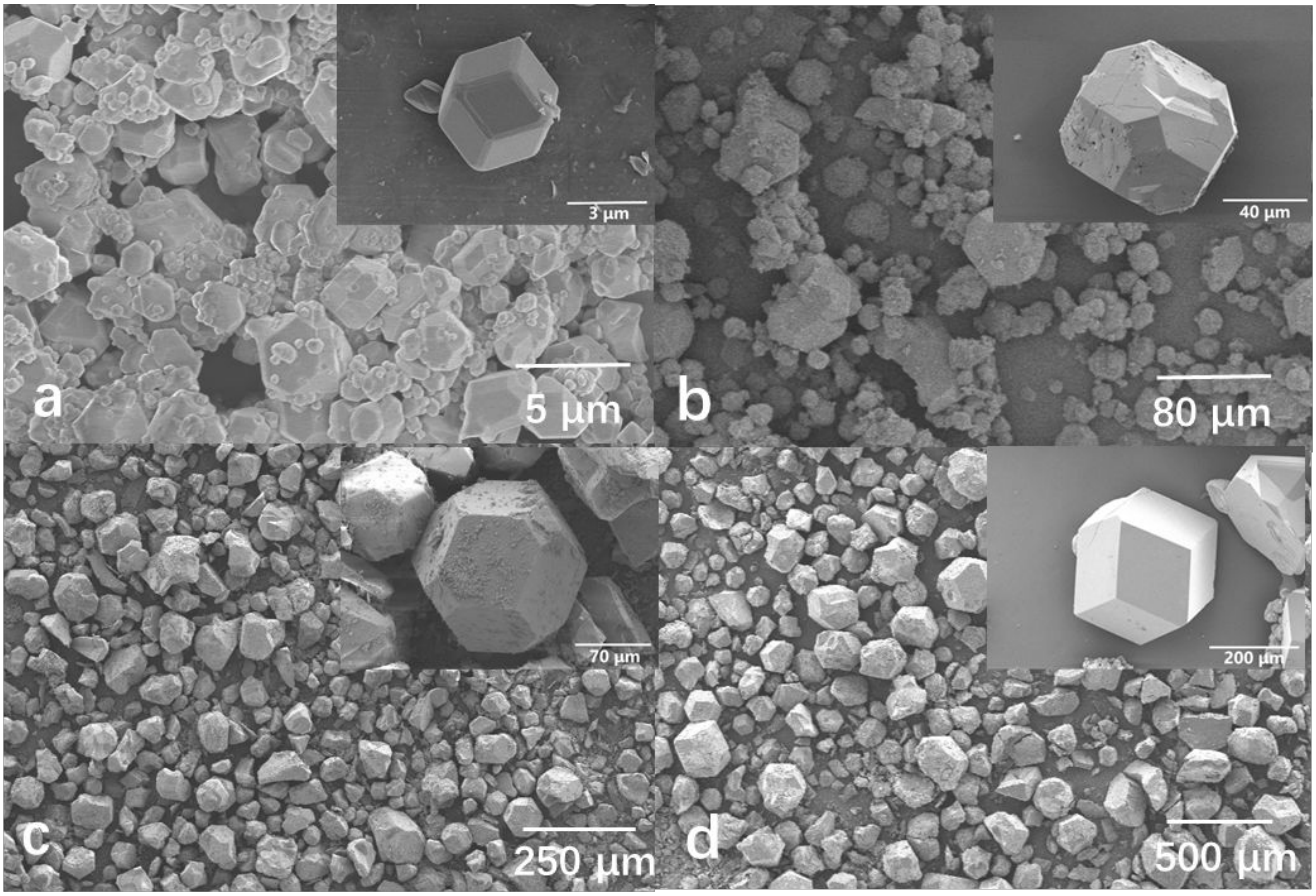

Figure S2. SEM images of ZIF-8-9 µm (a), ZIF-8-72 µm (b), ZIF-8-141 µm (c) and ZIF-8-224 µm (d).

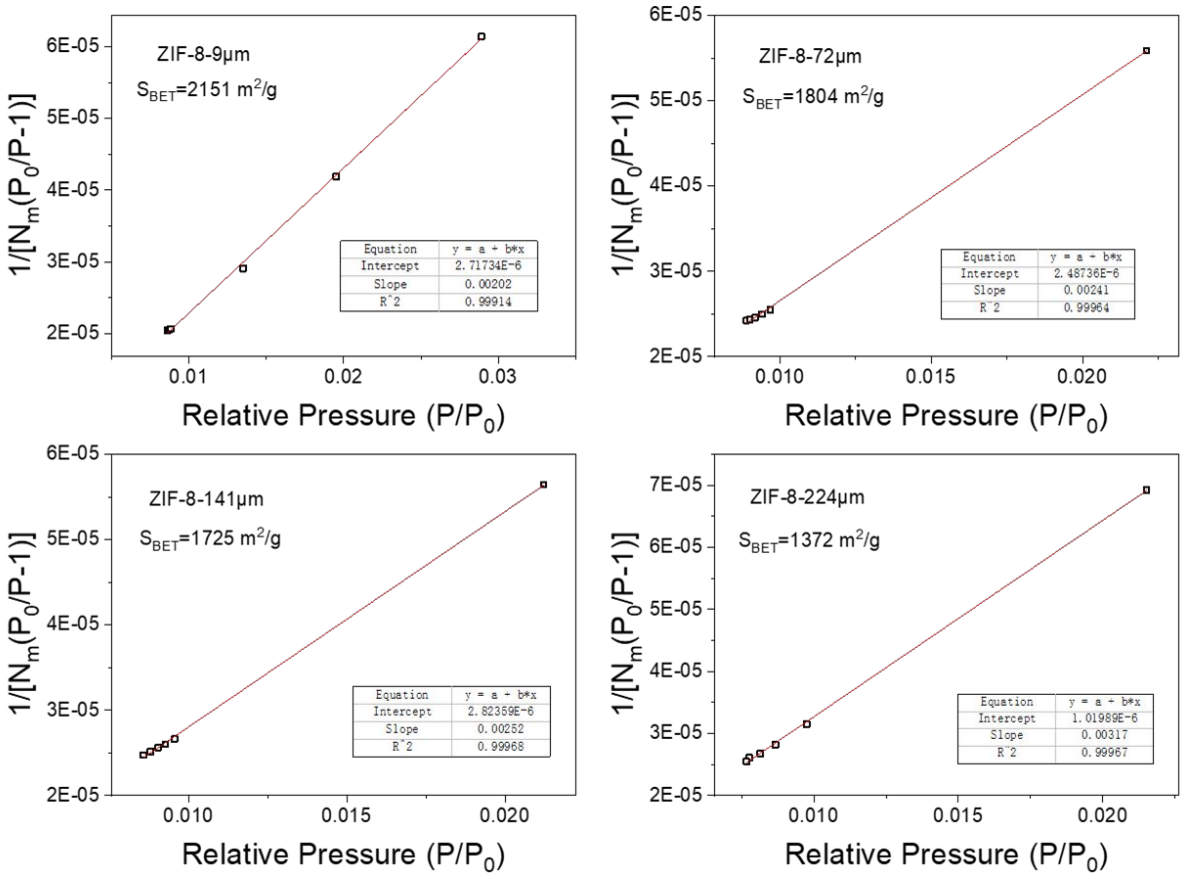

ZIF-8-9μm:

$$S_{BET} = \frac{1}{22414 \times (2.02 \times 10^{-3} + 2.72 \times 10^{-6})} \times 6.023 \times 10^{23} \times 0.162 \times 10^{-18} = 2151\ m^2/g$$

ZIF-8-72μm:

$$S_{BET} = \frac{1}{22414 \times (2.41 \times 10^{-3} + 2.49 \times 10^{-6})} \times 6.023 \times 10^{23} \times 0.162 \times 10^{-18} = 1804\ m^2/g$$

ZIF-8-141μm:

$$S_{BET} = \frac{1}{22414 \times (2.52 \times 10^{-3} + 2.82 \times 10^{-6})} \times 6.023 \times 10^{23} \times 0.162 \times 10^{-18} = 1725\ m^2/g$$

ZIF-8-224μm:

$$S_{BET} = \frac{1}{22414 \times (3.17 \times 10^{-3} + 1.02 \times 10^{-6})} \times 6.023 \times 10^{23} \times 0.162 \times 10^{-18} = 1372\ m^2/g$$

Figure S3. The BET surface area of ZIF-8-9 μm, ZIF-8-72 μm, ZIF-8-141 μm and ZIF-8-224 μm.

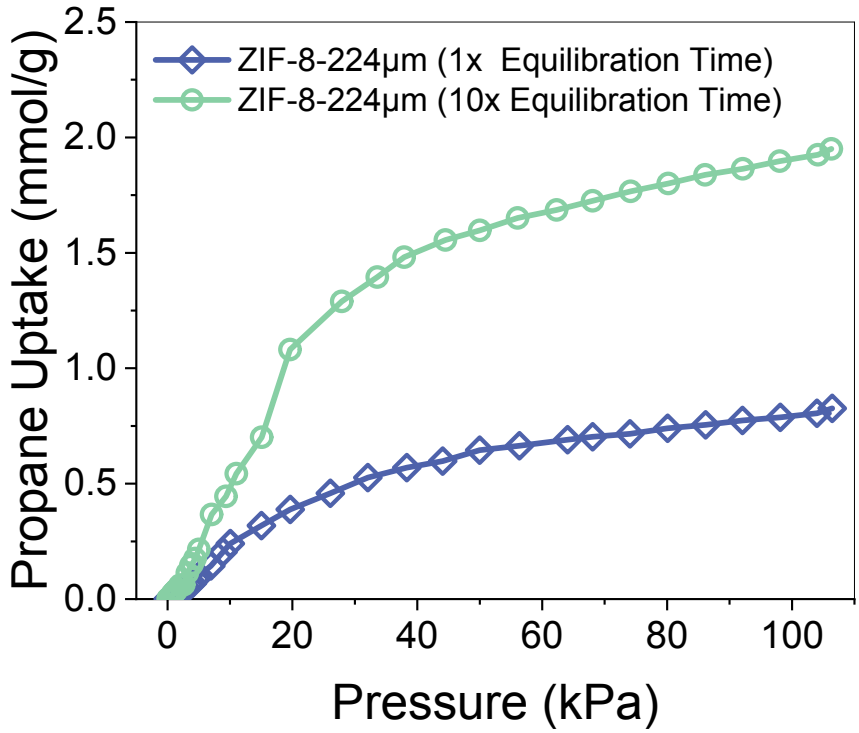

Figure S4. Propane adsorption isotherms of ZIF-8-224μm when the program is set to 1 or 10 times equilibration time.

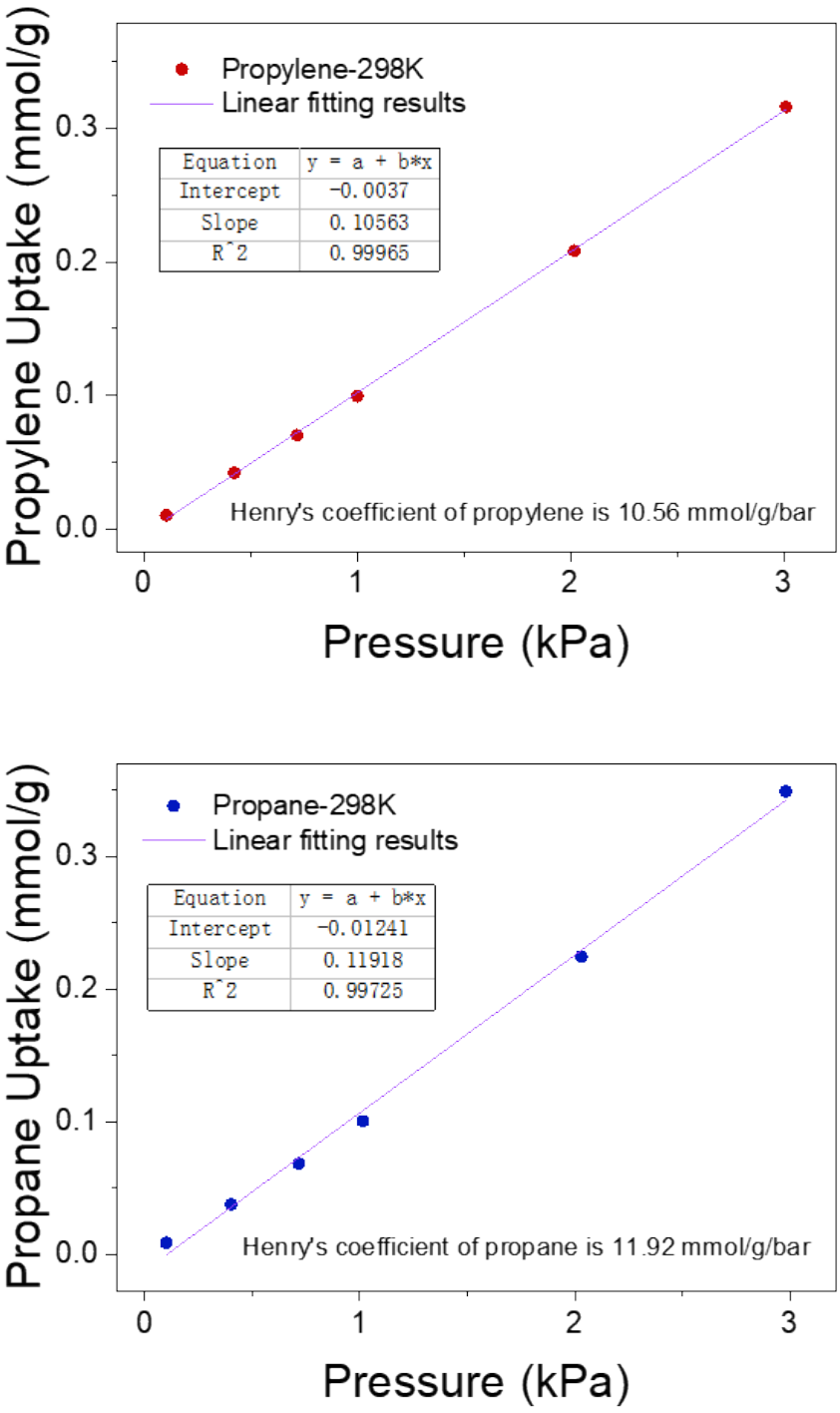

Figure S5. The single-component sorption isotherm of propylene and propane under low-pressure (<3.0 kPa) dealt with linear fitting.

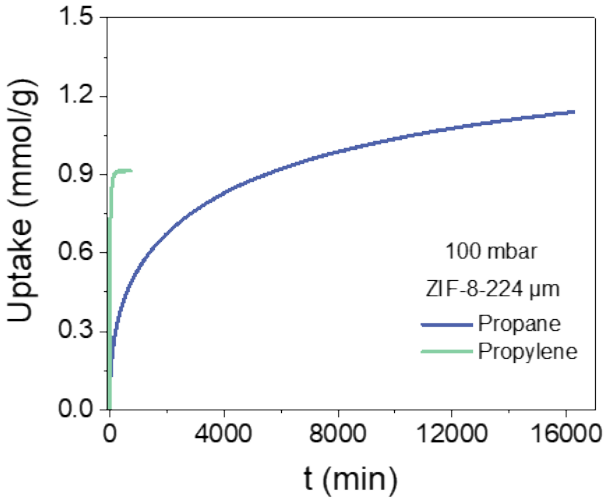
Uptake (mmol/g)
1.5
1.2
0.9
0.6
0.3
0.0
0
4000
8000
12000
16000
t (min)
100 mbar
ZIF-8-224 µm
Propane
Propylene

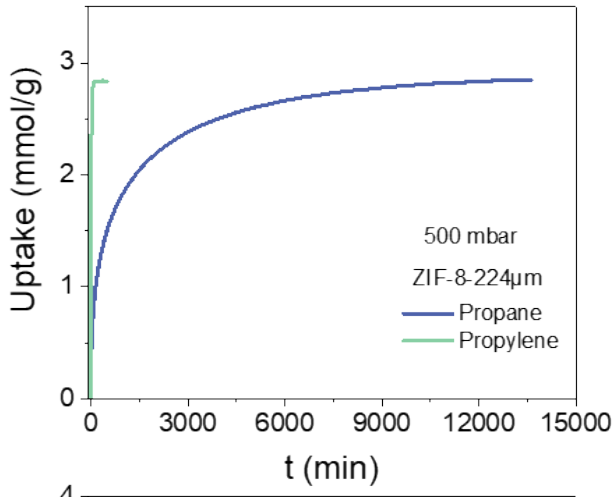
Uptake (mmol/g)
3
2
1
0
0
3000
6000
9000
12000
15000
t (min)
500 mbar
ZIF-8-224µm
Propane
Propylene

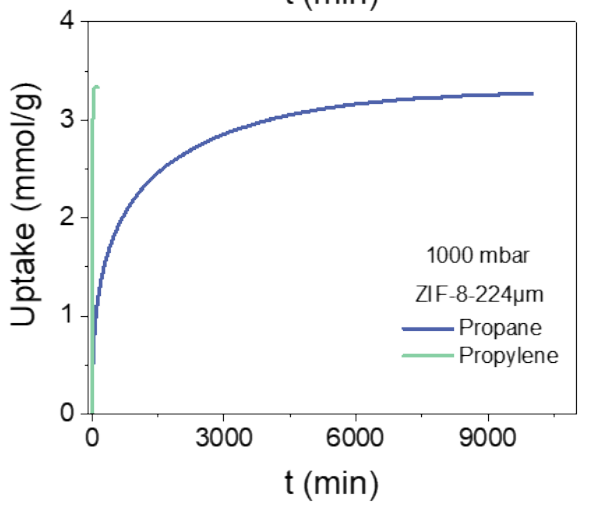
Uptake (mmol/g)
4
3
2
1
0
0
3000
6000
9000
t (min)
1000 mbar
ZIF-8-224µm
Propane
Propylene

Figure S6. Kinetic uptake plots of ZIF-8-224 μm under different pressures (100 mbar, 500 mbar, 1000 mbar) at 298 K.

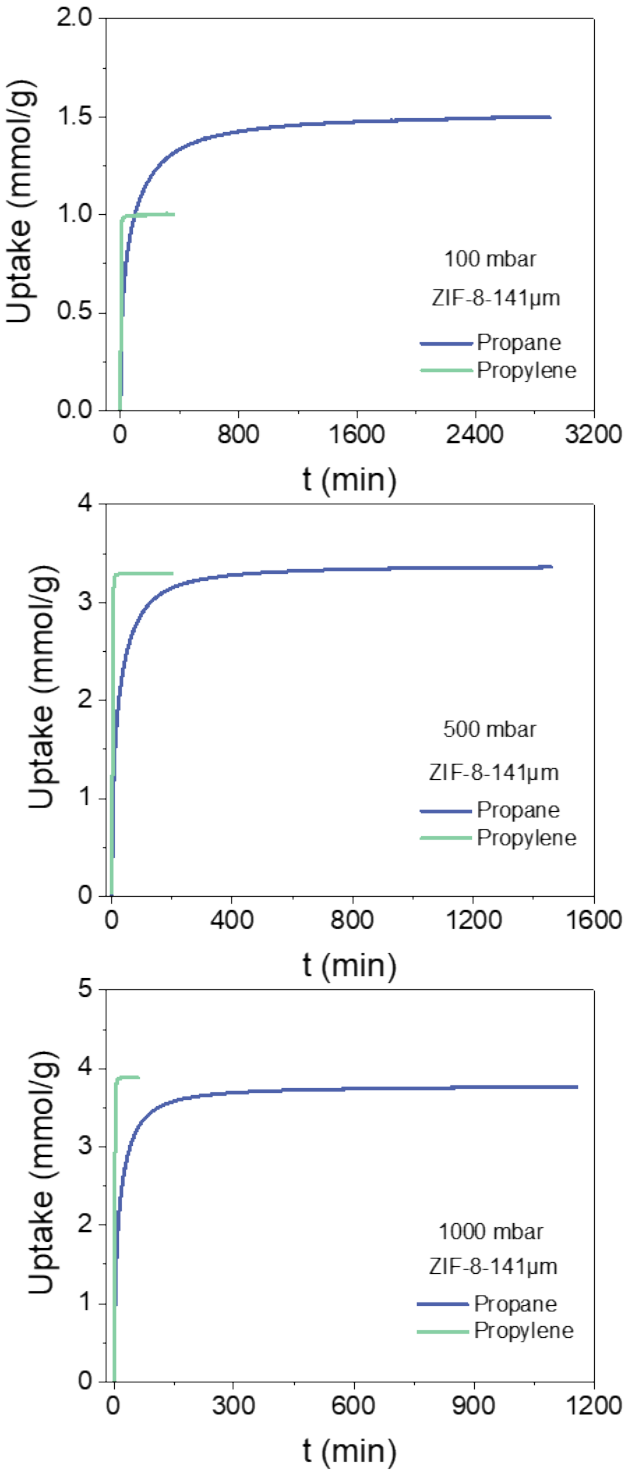

Figure S7. Kinetic uptake plots of ZIF-8-141 μm under different pressures (100 mbar, 500 mbar, 1000 mbar) at 298 K.

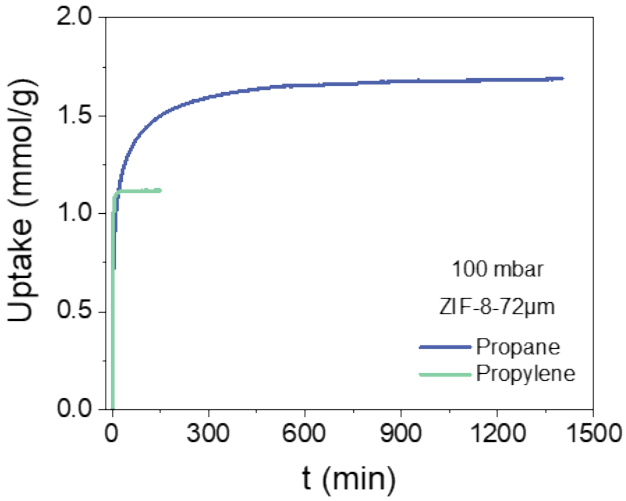
Uptake (mmol/g)
2.0
1.5
1.0
0.5
0.0
0
300
600
900
1200
1500
t (min)
100 mbar
ZIF-8-72µm
Propane
Propylene

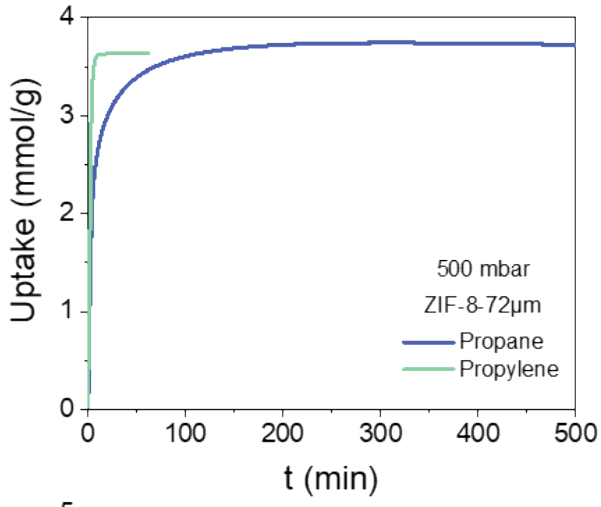
Uptake (mmol/g)
4
3
2
1
0
0
100
200
300
400
500
t (min)
500 mbar
ZIF-8-72µm
Propane
Propylene

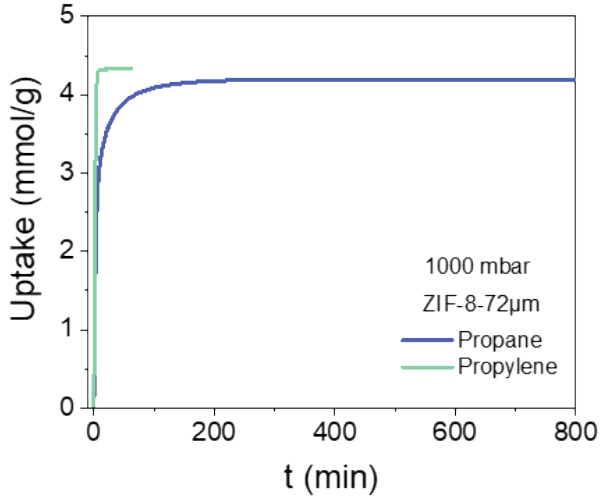
Uptake (mmol/g)
5
4
3
2
1
0
0
200
400
600
800
t (min)
1000 mbar
ZIF-8-72µm
Propane
Propylene

Figure S8. Kinetic uptake plots of ZIF-8-72 μm under different pressures (100 mbar, 500 mbar, 1000 mbar) at 298 K.

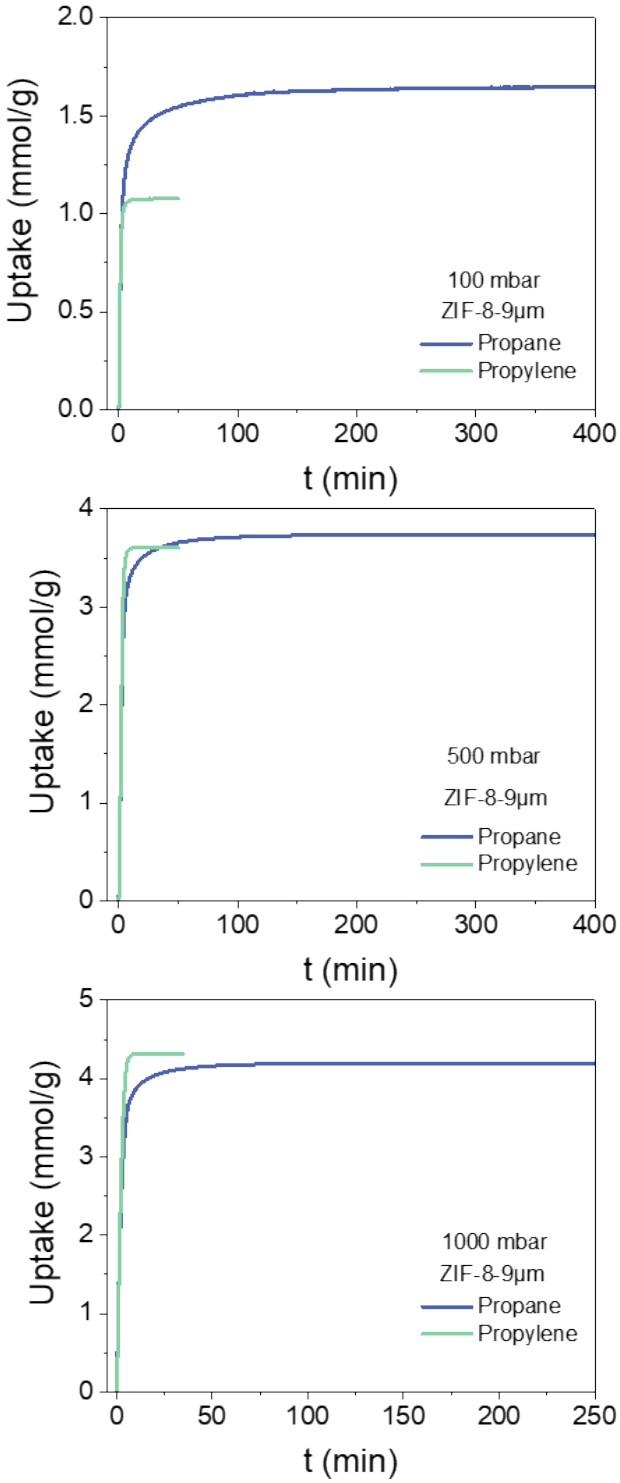

Figure S9. Kinetic uptake plots of ZIF-8-9 μm under different pressures (100 mbar, 500 mbar, 1000 mbar) at 298 K.

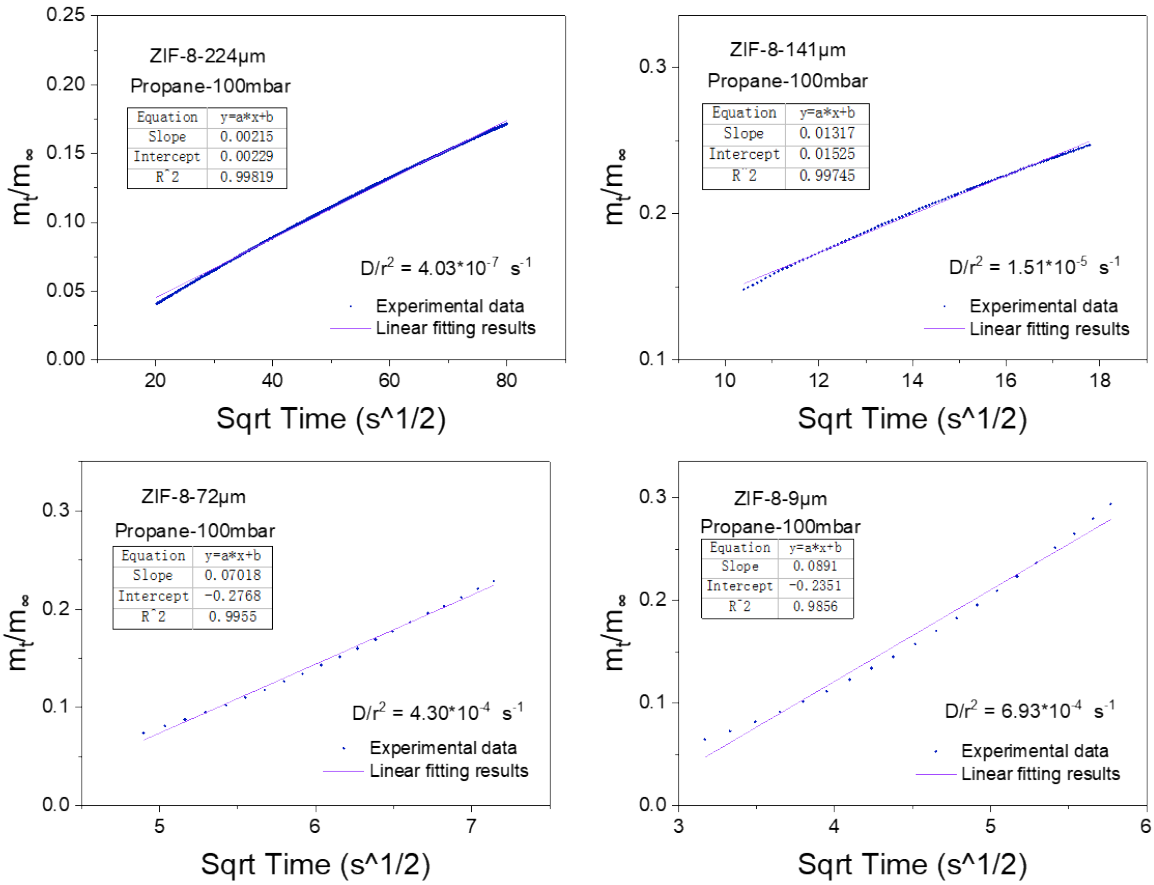

Figure S10. Fitting results of propane diffusion time constant for ZIF-8-9 μm, ZIF-8-72 μm, ZIF-8-141 μm and ZIF-8-224 μm.

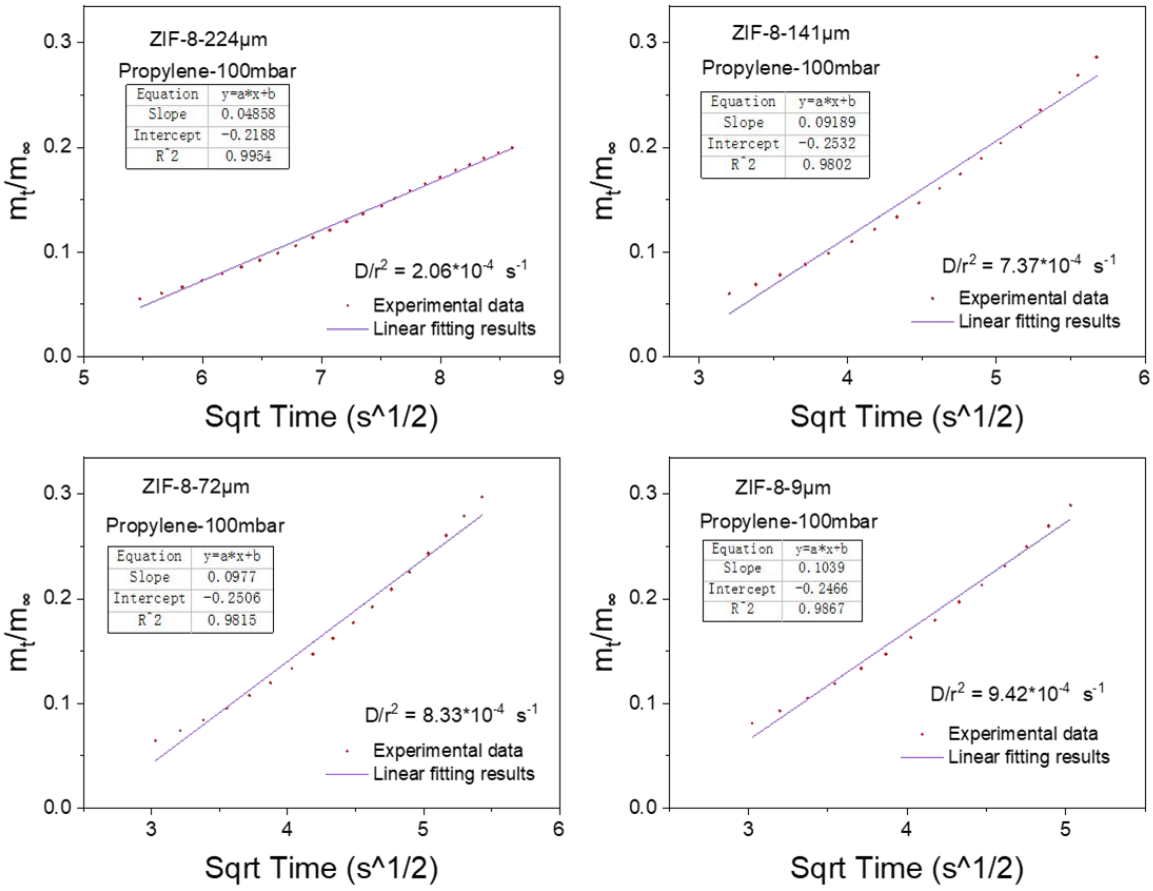

Figure S11. Fitting results of propylene diffusion time constant for ZIF-8-9 μm, ZIF-8-72 μm, ZIF-8-141 μm and ZIF-8-224 μm.

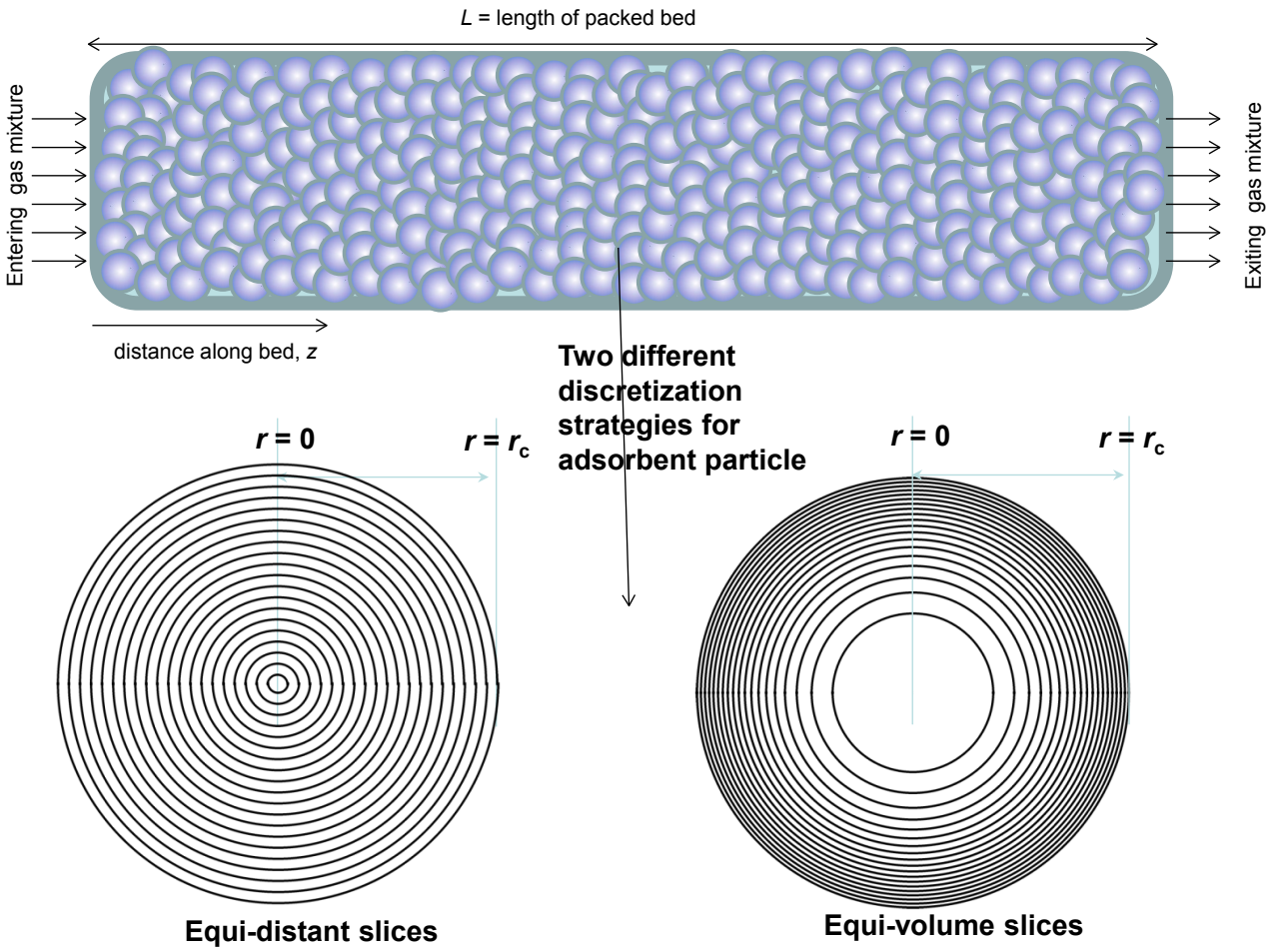

Figure S12. Two different discretization schemes for a single spherical crystallite.

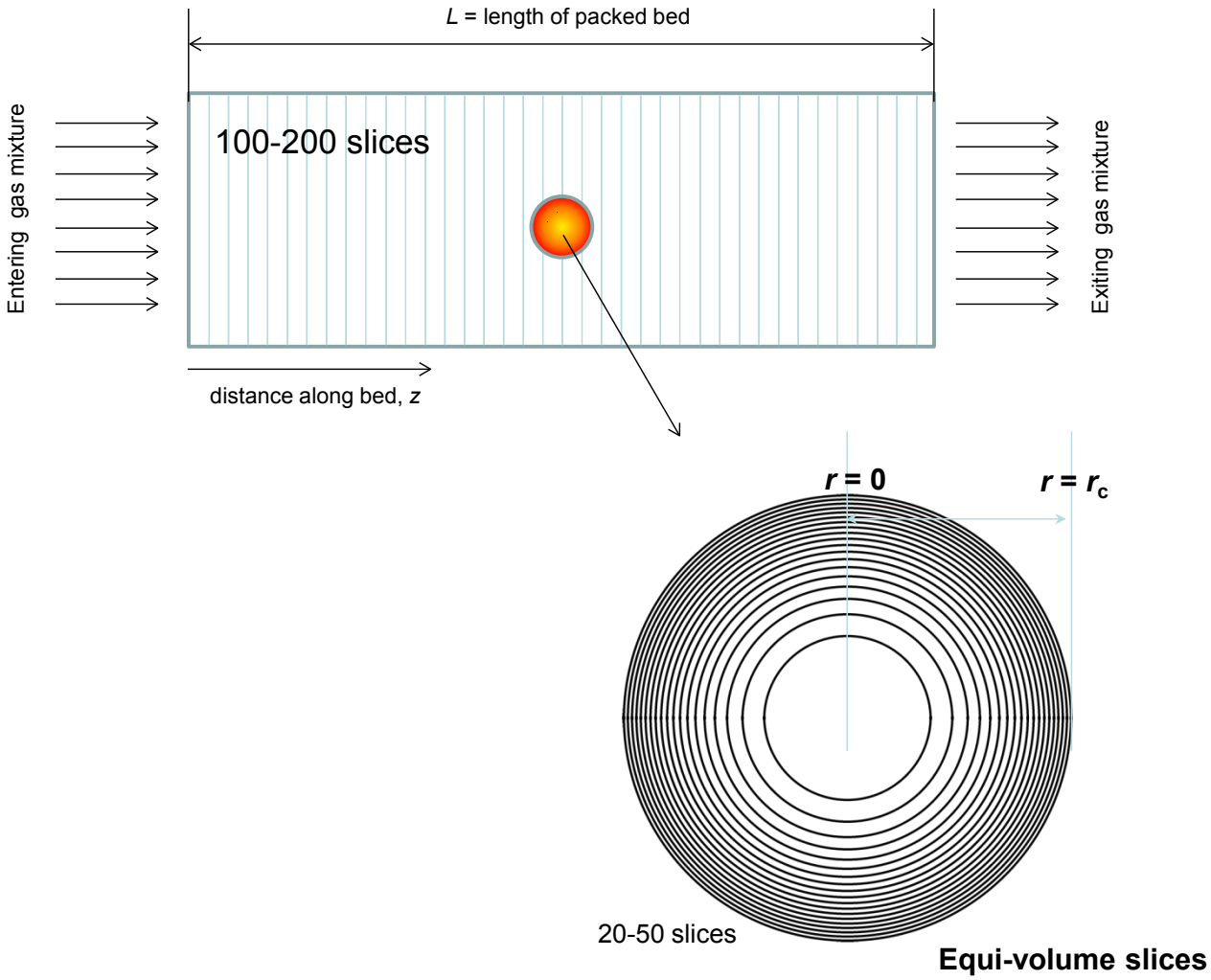

Figure S13. Discretization scheme for fixed bed adsorber.

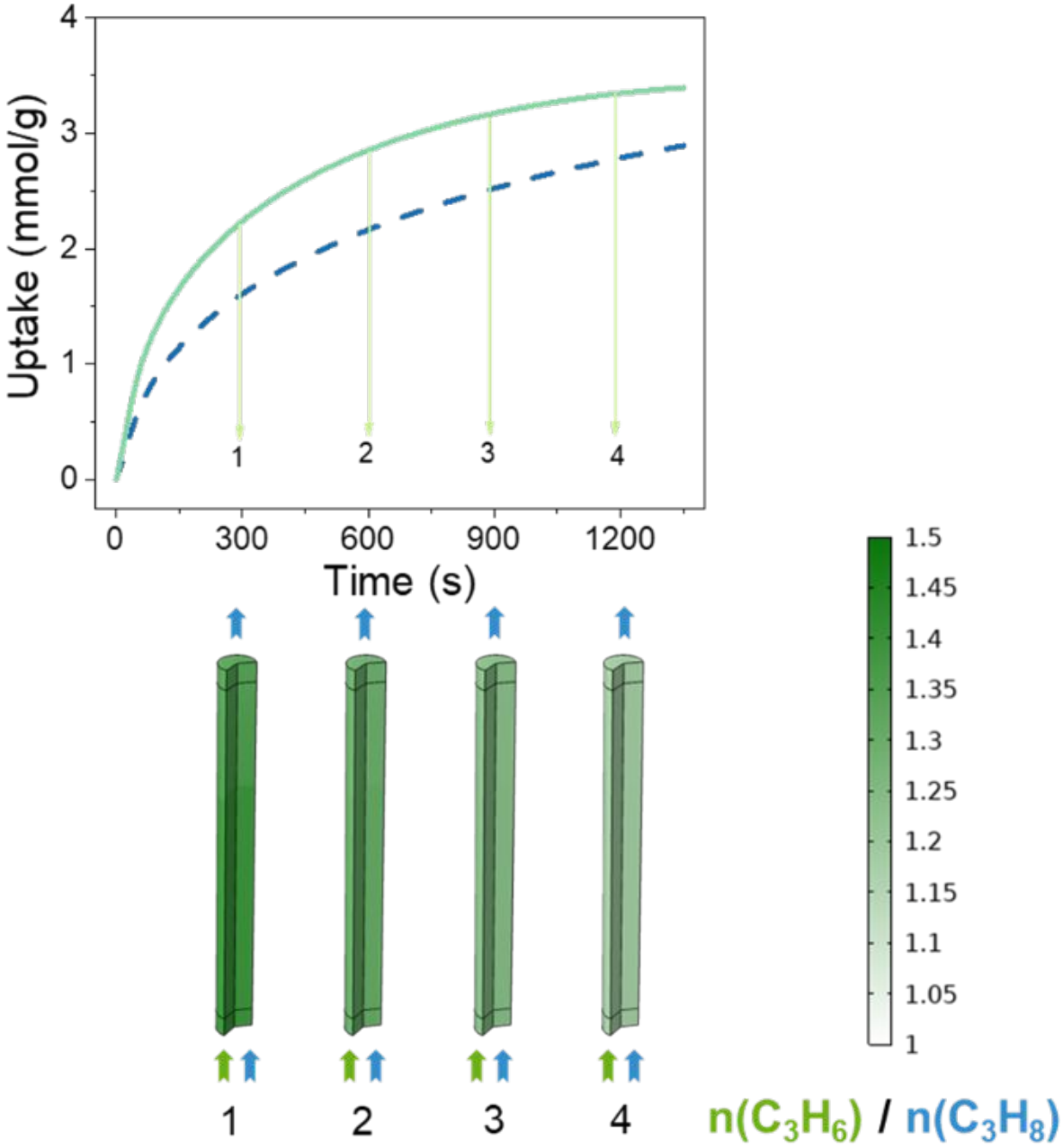

Figure S14. Breakthrough calculation results of ZIF-8-9 μm at the flow rate of 0.01 m/s. Upper part of the figure is the adsorption uptake-time curves of the fixed bed column (propane, blue dash-dot lines; propylene, green solid lines); Lower part of the figure is the adsorption capacity ratio of the fixed bed column at four specific times (300, 600, 900 and 1200 s).

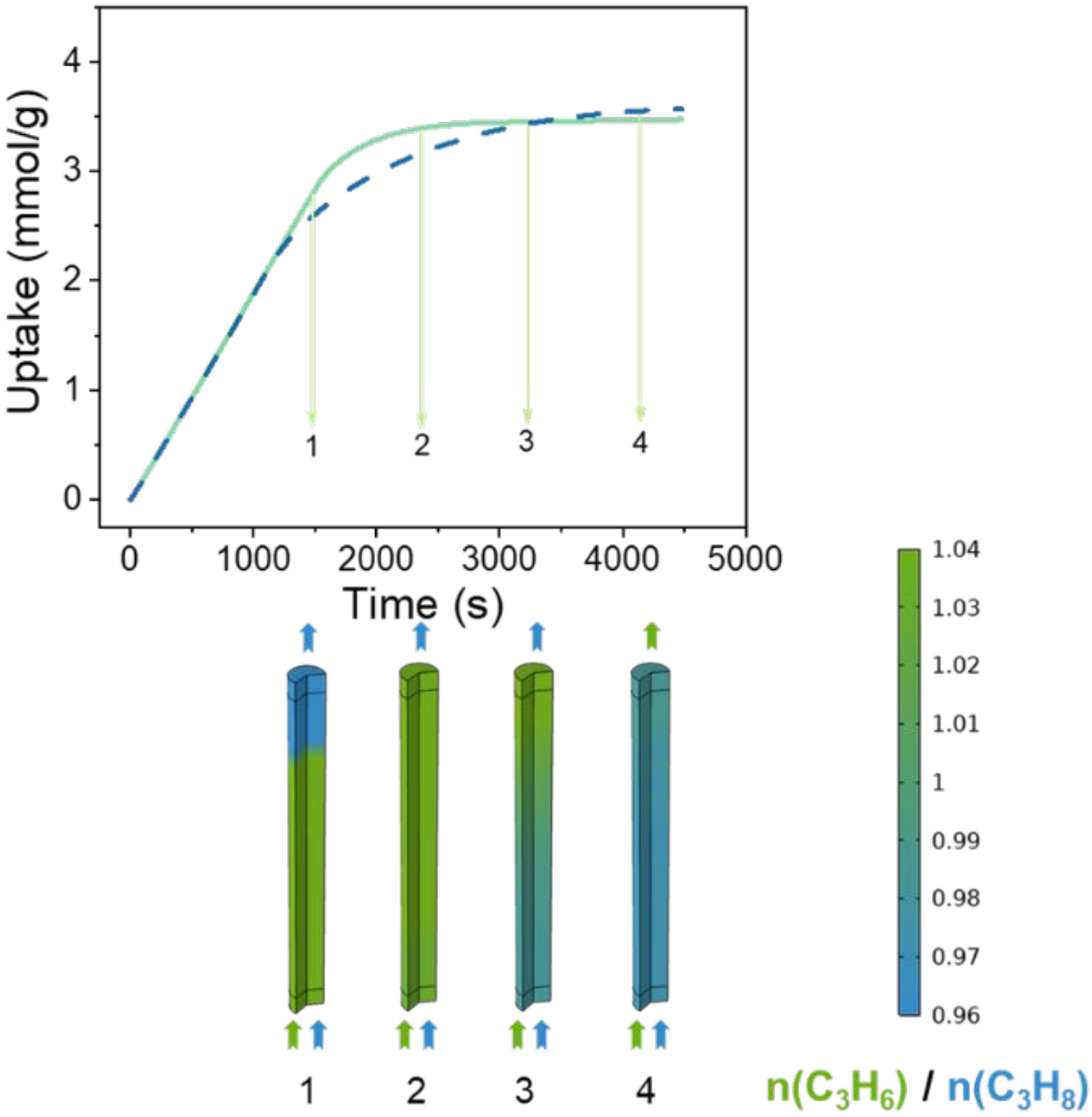

Figure S15. Breakthrough calculation results of ZIF-8-9 μm at the flow rate of 0.001 m/s. Upper part of the figure is the adsorption uptake-time curves of the fixed bed column (propane, blue dash-dot lines; propylene, green solid lines); Lower part of the figure is the adsorption capacity ratio of the fixed bed column at four specific times (1500, 2400, 3300 and 4200 s).

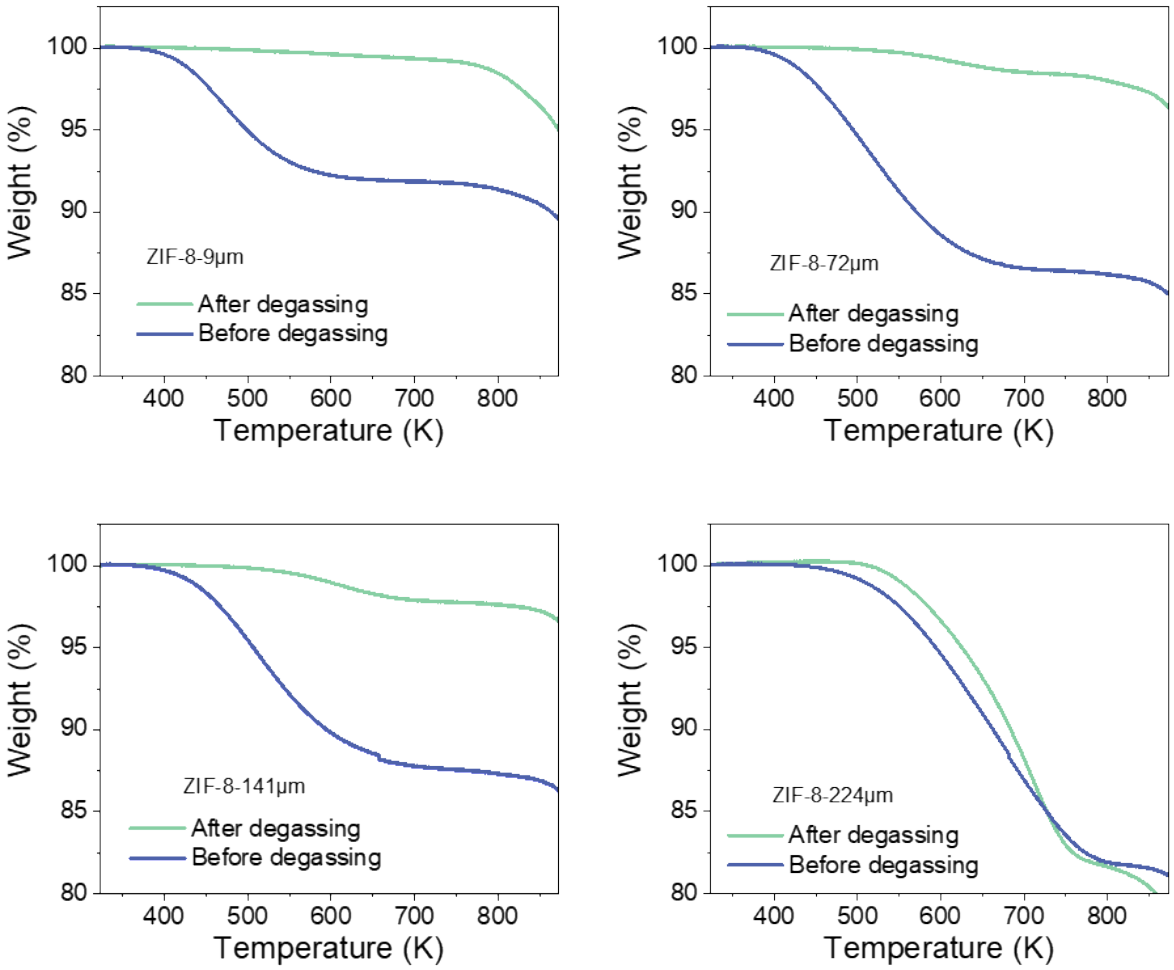

Figure S16. Thermogravimetric analysis results of ZIF-8-9 μm, ZIF-8-72 μm, ZIF-8-141 μm and ZIF-8-224 μm before/after degassing.

Table S1. Saturated adsorption capacity (mmol/g) of ZIF-8-9 μm, ZIF-8-72 μm, ZIF-8-141 μm and ZIF-8-224 μm calibrated by kinetic adsorption test at 100, 500 and 1000 mbar.

Material		**ZIF-8-9μm**	**ZIF-8-72μm**	**ZIF-8-141μm**	**ZIF-8-224μm**
Propane	**100 mbar**	1.66	1.69	1.50	1.14
	500 mbar	3.73	3.72	3.36	2.85
	1000 mbar	4.20	4.20	3.76	3.26
Propylene	**100 mbar**	1.08	1.12	1.00	0.91
	500 mbar	3.61	3.64	3.29	2.83
	1000 mbar	4.32	4.33	3.88	3.34

Table S2. Kinetic selectivity (D_{C3H6}/D_{C3H8} at 100 mbar, 298K) and diffusion time constant (D/r^2) of C_3H_6/C_3H_8 in ZIF-8-9 μm, ZIF-8-72 μm, ZIF-8-141 μm and ZIF-8-224 μm.

Material	D_{C3H6}/r^2 (s^{-1})	D_{C3H8}/r^2 (s^{-1})	D_{C3H6}/D_{C3H8}
ZIF-8-9μm	9.4×10^{-4}	6.9×10^{-4}	1.4
ZIF-8-72μm	8.3×10^{-4}	4.3×10^{-4}	1.9
ZIF-8-141μm	7.4×10^{-4}	1.5×10^{-5}	49.3
ZIF-8-224μm	2.1×10^{-4}	4.0×10^{-7}	525.0

Table S3. Breakthrough selectivity of ZIF-8-9 μm, ZIF-8-72 μm, ZIF-8-141 μm and ZIF-8-224 μm at the flow rate of 0.4 mL/min calculated from the ratio of adsorption amount obtained through breakthrough curve integration.

Material	Breakthrough Selectivity
ZIF-8-9μm	0.92
ZIF-8-72μm	1.07
ZIF-8-141μm	1.27
ZIF-8-224μm	2.02

Table S4. Breakthrough selectivity of ZIF-8-9 μm at the flow rate of 0.1, 0.2, 0.4, 1.7, 3.8 and 7.9 mL/min calculated from the ratio of adsorption amount obtained through breakthrough curve integration.

Flow rate (mL/min)	Breakthrough Selectivity
0.1	0.86
0.2	0.86
0.4	0.92
1.7	1.03
3.8	1.06
7.9	1.09

Table S5. Main parameters set in the fixed bed mass transfer model.

Name	Value	Description
$\mathbf{L_c}$	50 mm	Column length
$\mathbf{r_c}$	2.3 mm	Column radius
$\mathbf{d_p}$	9 μm, 224 μm	Particle diameter
$\mathbf{U_{column}}$	0.001 m/s, 0.01 m/s	Flow rate
$\mathbf{c_{A0}}$	20.2 mol/m^3	Propylene initial concentration
$\mathbf{c_{B0}}$	20.2 mol/m^3	Propane initial concentration
voi	0.55	Voidage
T	298 K	System temperature
ρ	1.758 kg/m^3	Mixture density
η	8.12E-6 Pa·s	Mixture viscosity
$\mathbf{p_{ref}}$	1 atm	Reference pressure

References

1. Krishna, R. Screening Metal-Organic Frameworks for Mixture Separations in Fixed-Bed Adsorbers using a Combined Selectivity/Capacity Metric. *RSC Advances* **2017,** *7*, 35724-35737.
2. Krishna, R. Methodologies for Evaluation of Metal-Organic Frameworks in Separation Applications. *RSC Advances* **2015,** *5*, 52269-52295.
3. Krishna, R. The Maxwell-Stefan Description of Mixture Diffusion in Nanoporous Crystalline Materials. *Microporous Mesoporous Mater.* **2014,** *185*, 30-50.
4. Krishna, R. Tracing the Origins of Transient Overshoots for Binary Mixture Diffusion in Microporous Crystalline Materials. *Phys. Chem. Chem. Phys.* **2016,** *18*, 15482-15495.
5. Krishna, R. Synergistic and Antisynergistic Intracrystalline Diffusional Influences on Mixture Separations in Fixed Bed Adsorbers. *Precision Chemistry* **2023,** *1*, 83-93.
6. Krishna, R.; Baur, R. Modelling Issues in Zeolite Based Separation Processes. *Sep. Purif. Technol.* **2003,** *33*, 213-254.
7. Krishna, R.; Baur, R. Diffusion, Adsorption and Reaction in Zeolites: Modelling and Numerical Issues. http://krishna.amsterchem.com/zeolite/ (accessed 17 April 2020).
8. Ruthven, D. M.; Farooq, S.; Knaebel, K. S. *Pressure swing adsorption*. VCH Publishers: New York, 1994.
9. Krishna, R. Describing the Diffusion of Guest Molecules inside Porous Structures. *J. Phys. Chem. C* **2009,** *113*, 19756-19781.
10. Krishna, R. Diffusion in Porous Crystalline Materials. *Chem. Soc. Rev.* **2012,** *41*, 3099-3118.
11. Krishna, R. Highlighting the Influence of Thermodynamic Coupling on Kinetic Separations with Microporous Crystalline Materials. *ACS Omega* **2019,** *4*, 3409-3419.
12. Krishna, R. Occupancy Dependency of Maxwell−Stefan Diffusivities in Ordered Crystalline Microporous Materials. *ACS Omega* **2018,** *3*, 15743-15753.
13. Krishna, R. Thermodynamically Consistent Methodology for Estimation of Diffusivities of Mixtures of Guest Molecules in Microporous Materials. *ACS Omega* **2019,** *4*, 13520-13529.
14. Krishna, R. A Maxwell-Stefan-Glueckauf Description of Transient Mixture Uptake in Microporous Adsorbents. *Sep. Purif. Technol.* **2018,** *191*, 392-399.
15. Krishna, R. Maxwell-Stefan Modelling of Mixture Desorption Kinetics in Microporous Crystalline Materials. *Sep. Purif. Technol.* **2019,** *229*, 115790.
16. Myers, A. L.; Prausnitz, J. M. Thermodynamics of Mixed Gas Adsorption. *A.I.Ch.E.J.* **1965,** *11*, 121-130.
17. Krishna, R.; van Baten, J. M. Investigating the potential of MgMOF-74 membranes for CO_2 capture. *J. Membr. Sci.* **2011,** *377*, 249-260.
18. He, Y.; Krishna, R.; Chen, B. Metal-Organic Frameworks with Potential for Energy-Efficient Adsorptive Separation of Light Hydrocarbons. *Energy Environ. Sci.* **2012,** *5*, 9107-9120.
19. Durlofsky, L.; Brady, J. Analysis of the Brinkman equation as a model for flow in porous media. *The Physics of fluids* **1987,** *30* (11), 3329-3341.

20. Neale, G.; Nader, W. Practical significance of Brinkman's extension of Darcy's law: coupled parallel flows within a channel and a bounding porous medium. *The Canadian Journal of Chemical Engineering* **1974,** *52* (4), 475-478.
21. Costa, A. Permeability‐porosity relationship: A reexamination of the Kozeny‐Carman equation based on a fractal pore‐space geometry assumption. *Geophysical research letters* **2006,** *33* (2).
22. Xu, P.; Yu, B. Developing a new form of permeability and Kozeny–Carman constant for homogeneous porous media by means of fractal geometry. *Advances in water resources* **2008,** *31* (1), 74-81.
23. Millington, R.; Quirk, J. Permeability of porous solids. *Transactions of the Faraday Society* **1961,** *57*, 1200-1207.
24. Narin, G.; Martins, V. F.; Campo, M.; Ribeiro, A. M.; Ferreira, A.; Santos, J. C.; Schumann, K.; Rodrigues, A. E. Light olefins/paraffins separation with 13X zeolite binderless beads. *Separation and Purification Technology* **2014,** *133*, 452-475.
25. Qasem, N. A.; Ben-Mansour, R. Adsorption breakthrough and cycling stability of carbon dioxide separation from CO2/N2/H2O mixture under ambient conditions using 13X and Mg-MOF-74. *Applied Energy* **2018,** *230*, 1093-1107.
26. Saha, D.; Orkoulas, G.; Chen, J.; Hensley, D. K. Adsorptive separation of CO2 in sulfur-doped nanoporous carbons: Selectivity and breakthrough simulation. *Microporous and Mesoporous Materials* **2017,** *241*, 226-237.